bioRxiv preprint doi: https://doi.org/10.1101/2020.08.25.256339; this version posted August 26, 2020. The copyright holder for this preprint (which was not certified by peer review) is the author/funder, who has granted bioRxiv a license to display the preprint in perpetuity. It is made available under aCC-BY-NC-ND 4.0 International license.

Highly potent anti-SARS-CoV-2 multi-DARPin therapeutic candidates

Marcel Walser[1,*], Sylvia Rothenberger[2,3,*], Daniel L. Hurdiss[4,5,*], Anja Schlegel[1], Valérie Calabro[1], Simon Fontaine[1], Denis Villemagne[1], Maria Paladino[1], Tanja Hospodarsch[1], Alexandra Neculcea[1], Andreas Cornelius[1], Patricia Schildknecht[1], Mirela Matzner[1], Martin Hänggi[1], Marco Franchini[1], Yvonne Kaufmann[1], Iris Schlegel[1], Chloe Iss[1], Thamar Loser[1], Susanne Mangold[1], Christel Herzog[1], Dieter Schiegg[1], Christian Reichen[1], Filip Radom[1], Andreas Bosshart[1], Andreas Lehmann[1], Micha A. Haeuptle[1], Alexander Zürcher[1], Toni Vagt[1], Gabriel Sigrist[1], Marcel Straumann [1], Karl Proba[1], Niina Veitonmäki[1], Keith M. Dawson[1], Christof Zitt[1], Jennifer Mayor[2,3], Sarah Ryter[2], Heyrhyoung Lyoo[4], Chunyan Wang[4], Wentao Li[4], Ieva Drulyte[6], H. Kaspar Binz[7], Leon de Waal[8], Koert J. Stittelaar[8], Seth Lewis[1], Daniel Steiner[1], Frank J.M. van Kuppeveld[4], Olivier Engler[2], Berend-Jan Bosch[4], Michael T. Stumpp[1,9], Patrick Amstutz [1]

*These authors contributed equally to this work

[1]Molecular Partners AG, Wagistrasse 14, 8952 Zurich-Schlieren, Switzerland

[2]Spiez Laboratory, Austrasse, 3700 Spiez, Switzerland

[3]Institute of Microbiology, University Hospital Center and University of Lausanne, Rue du Bugnon 48, 1011 Lausanne, Switzerland

[4]Department Biomolecular Health Sciences, Division Infectious Diseases & Immunology - Virology section, Faculty of Veterinary Medicine, Utrecht University, 3584CL Utrecht, The Netherlands.

[5]Cryo-Electron Microscopy, Bijvoet Center for Biomolecular Research, Department of Chemistry, Faculty of Science, Utrecht University, Padualaan 8, 3584 CH Utrecht, The Netherlands

[6]Materials and Structural Analysis, Thermo Fisher Scientific, Eindhoven, 5651 GG, The Netherlands.

[7]Binz Biotech Consulting, Lüssirainstrasse 52, 6300 Zug

[8]Viroclinics Xplore, Landerd Campus, Nistelrooise Baan 3, 5374 RE Schaijk, The Netherlands

[9]To whom correspondence should be addressed:

Michael T. Stumpp

+41 44 755 77 00

info@molecularpartners.com

Keywords: SARS-CoV-2, COVID-19, corona virus, antiviral therapy, post-exposure prophylaxis, DARPin® drug, ankyrin repeat protein, multi-specific, ribosome display

DARPin® is a registered trademark owned by Molecular Partners AG

bioRxiv preprint doi: https://doi.org/10.1101/2020.08.25.256339; this version posted August 26, 2020. The copyright holder for this preprint (which was not certified by peer review) is the author/funder, who has granted bioRxiv a license to display the preprint in perpetuity. It is made available under aCC-BY-NC-ND 4.0 International license.

Abstract

Globally accessible preventive and therapeutic molecules against SARS-CoV-2 are urgently needed. DARPin molecules are an emerging class of novel therapeutics based on naturally occurring repeat proteins (~15 kDa in size) and can be rapidly produced in bacteria in large quantities. Here, we report the identification of 380 DARPin molecules specifically targeting the SARS-CoV-2 spike protein selected from a naïve library of 10^{12} DARPin molecules. Using extensive biophysical and biochemical characterization, (pseudo)virus neutralization assays and cryo-EM analysis, 11 mono-DARPin molecules targeting either the receptor binding domain (RBD), the S1 N-terminal-domain (NTD) or the S2 domain of the SARS-CoV-2 spike protein were chosen. Based on these 11 mono-DARPin molecules, 31 anti-SARS-CoV-2 multi-DARPin molecules were constructed which can broadly be grouped into 2 types; multi-paratopic RBD-neutralizing DARPin molecules and multi-mode DARPin molecules targeting simultaneously RBD, NTD and the S2 domain. Each of these multi-DARPin molecules acts by binding with 3 DARPin modules to the SARS-CoV-2 spike protein, leading to potent inhibition of SARS-CoV-2 infection down to 1 ng/ml (12 pM) and potentially providing protection against viral escape mutations. Additionally, 2 DARPin modules binding serum albumin, conferring an expected half-life of about 3 weeks in humans, were included in the multi-DARPin molecules. The protective efficacy of one multi-DARPin molecule was studied in a Golden Syrian hamster SARS-CoV-2 infection model, resulting in a significant reduction in viral load and pathogenesis. In conclusion, the multi-DARPin molecules reported here display very high antiviral potency, high-production yield, and a long systemic half-life, and thereby have the potential for single-dose use for prevention and treatment of COVID-19.

bioRxiv preprint doi: https://doi.org/10.1101/2020.08.25.256339; this version posted August 26, 2020. The copyright holder for this preprint (which was not certified by peer review) is the author/funder, who has granted bioRxiv a license to display the preprint in perpetuity. It is made available under aCC-BY-NC-ND 4.0 International license.

Introduction

Fighting the COVID-19 pandemic will require coordinated global efforts to maximize the benefits of vaccinations and therapeutics[1]. Even though vaccine efforts have progressed considerably, there is and will be a remaining medical need for (preventive) therapeutics to treat patients and to protect health care workers as well as other vulnerable people who cannot get protected by vaccination. Neutralizing monoclonal antibodies are expected to be critically important and could be readily available[2-4], however they are complex to manufacture and come at a considerable cost, meaning poor countries may be priced out[5], thus preventing an effective global solution.

DARPin molecules are an emerging class of novel therapeutics that are actively being developed in ophthalmology and oncology, with four molecules at a clinical stage[6]. Here, we report the generation and characterization of the first anti-viral DARPin molecules in the context of the COVID-19 pandemic. DARPin molecules are derived from naturally occurring ankyrin repeat proteins (Supplementary Figure 1a). To generate therapeutic DARPin molecules, a pure *in vitro* approach (i.e. selections via ribosome display) is possible and can be carried out in a very short time frame, only requiring the target protein, in this case the SARS-CoV-2 spike protein or subdomains thereof. Hence, therapeutic DARPin molecules can be prepared independently of patient samples and the availability of neutralizing antibodies from those patients. DARPin molecules can be mono-specific or linked by peptide linkers to form multi-DARPin molecules with several specificities (Supplementary Figure 1b). Notably, DARPin molecules can be manufactured by microbial fermentation, and thus be potentially available world-wide within a short time due to lower technical requirements to provide large-scale clinical grade material. Additionally, DARPin molecules are relatively heat-stable, thus offering the prospect of a reduced cold chain for distribution around the globe.

The SARS-CoV-2 spike protein[7-11], which is responsible for virus entry into the host cell, comprises multiple functional units: S1, which includes the N-terminal domain (NTD) and the receptor binding domain (RBD) responsible for interaction with host receptors[10] such as angiotensin-converting enzyme 2 (ACE2), and the S2 domain, which is responsible for virus-host cell membrane fusion by triggering conformational changes. Priming of the fusion function is thought to occur via cleavage of S2 by host proteases during cell entry[12,13]. Consequently, this presents the opportunity to target several sites on a single viral protein, leading to multiple mechanisms of inhibition. Such a multi-pronged approach is therefore expected to lead to higher potencies (lower doses required) and better protection against potential viral escape mutations.

bioRxiv preprint doi: https://doi.org/10.1101/2020.08.25.256339; this version posted August 26, 2020. The copyright holder for this preprint (which was not certified by peer review) is the author/funder, who has granted bioRxiv a license to display the preprint in perpetuity. It is made available under aCC-BY-NC-ND 4.0 International license.

With most antibody approaches focusing on one or two epitopes of the SARS-CoV-2 spike protein, we present here a novel approach using DARPin molecules to simultaneously bind the SARS-CoV-2 spike protein at three sites with one molecule. The results reported below describe the selection and characterization of mono-specific DARPin molecules against various parts of the spike protein, how we chose the most potent mono-DARPin molecules and, supported by cryoEM data, rationally combined them into highly potent multi-DARPin molecules. Importantly, we demonstrate that multi-DARPin molecules can prevent disease in a hamster model of COVID-19. We anticipate that antiviral multi-DARPin molecules represent an easy-to-deploy antiviral approach to treat and/or prevent COVID-19.

bioRxiv preprint doi: https://doi.org/10.1101/2020.08.25.256339; this version posted August 26, 2020. The copyright holder for this preprint (which was not certified by peer review) is the author/funder, who has granted bioRxiv a license to display the preprint in perpetuity. It is made available under aCC-BY-NC-ND 4.0 International license.

Results

Selection and characterization of mono-DARPin molecules targeting different regions of SARS-CoV-2 spike.

The DARPin technology is based on naïve DARPin libraries[6], with a physical diversity of about 10^{12} different mono-DARPin molecules, allowing the selection of sets of very diverse binding molecules by ribosome display[14,15], the method of choice when dealing with libraries of such large diversities. DARPin libraries are based on a consensus design approach using several hundred ankyrin repeat protein sequences of the human and mouse genome[16]. An overview of the entire generation process of anti-SARS-CoV-2 spike protein binding DARPin molecules is shown in Figure 1. To obtain individual DARPin molecules binding to various parts of the SARS-CoV-2 spike protein and potentially inhibiting viral cell entry, the generation was focused on DARPin molecules binding to the receptor binding domain (RBD), the S1 N-terminal domain (NTD) or the S2 domain[17]. In order to focus on the most potently binding DARPin molecules obtained after four ribosome display selection rounds, *E. coli* cell extracts overexpressing 3'420 individual DARPin molecules were screened by homogeneous time-resolved fluorescence (HTRF) assays for binding to different spike protein domains. A total of 909 binding DARPin molecules were selected based on binding and inhibition profiles obtained in HTRF. Using the knowledge of which domain the mono-DARPin molecules bound to, 380 DARPin molecules were chosen to be expressed in 96-well format and purified to homogeneity. In parallel, the DNA sequences were determined, which confirmed a high level of sequence diversity. DARPin molecules were further characterized for antiviral potency in a VSV-pseudovirion neutralization assay (PsV NA) as well as biophysically by size exclusion chromatography (SEC), Sypro-Orange thermal stability assessment[18], ProteOn surface plasmon resonance (SPR) target affinity assessment, and ELISA, to orthogonally evaluate target binding, as well as a HTRF-based RBD/human ACE2 binding competition experiments which was developed in-house. In parallel to the characterization of the 380 mono-DARPin molecules, 6 mono-DARPin molecules of known specificity were used to randomly assemble a set of 192 Tri-DARPin molecules. The assessment of antiviral potency of this set of randomly assembled Tri-DARPin molecules proved, as envisioned, to have increased anti-viral potencies, but also provided valuable information on how the binders to various spike protein domain need to be combined. This guided the rational assembly of multi-DARPin molecules described below (data not shown).

Based on the combined data for the 380 mono-DARPin molecules, 11 of them (Table 1 and Supplementary Figure 4) were chosen for the rational generation of 31 multi-DARPin molecules (Table 2) described below. Each of these 11 mono-specific DARPin molecules displayed low pM to low nM affinities and had a different binding surface to potentially increase the resistance against future SARS-CoV-2 mutations.

bioRxiv preprint doi: https://doi.org/10.1101/2020.08.25.256339; this version posted August 26, 2020. The copyright holder for this preprint (which was not certified by peer review) is the author/funder, who has granted bioRxiv a license to display the preprint in perpetuity. It is made available under aCC-BY-NC-ND 4.0 International license.

Cryo-EM analysis of mono-DARPin molecules

To gain further insights into the mode of inhibition and binding, 3 individual mono-DARPin molecules targeting RBD, S1-NTD, or S2, were subjected to cryo-electron microscopy (cryo-EM) analysis in complex with the trimeric spike ectodomain. In each case, few intact spikes remained following incubation with the mono-DARPin molecules, particularly with the S2 binder. When spike ectodomains were incubated with RBD-binding mono-DARPin molecule #3 for 15 seconds prior to vitrification, 3D classification revealed that 65% of the intact S ectodomains were in the closed conformation, 20% had two RBDs in the open conformation and 15% had all three RBDs in the open conformation (Supplementary Figure 2a). For the open RBD classes, additional density, consistent with the size of a mono-DARPin molecule, was present on the RBD receptor binding ridge (RBR). When the incubation time was increased to 60 seconds, all the S ectodomains had two or three RBDs in the open conformation (Supplementary Figure 2b). This demonstrates that DARPin binding prevents closure of the RBD through a previously described ratcheting mechanism[17]. Subsequent 3D refinement of the fully open class, from the 60 second incubated sample, produced a 6.9 Å global resolution map (Figure 2a and Supplementary Figure 2c-d). The resolution of the map was sufficient to unambiguously assign the pose of RBD-binding mono-DARPin molecule #3, which binds perpendicular to the RBD receptor binding motif (RBM), with its N-terminus orientated toward the spike three-fold symmetry axis. The concave DARPin binding surface covers the RBR and overlaps with the ACE2 binding site (Figure 2b). Based on the cryo-EM data, molecular docking experiments were performed. The top scoring model indicated that the interface area is ~700 $Å^2$ and that key epitope residues are F456, Y473, F486, N487 and Y489 , which form a primarily hydrophobic interface with the DARPin molecule #3 (Supplementary Figure 2e). The proposed model is in line with 30 pM binding affinity measured in SPR. Taken together, these data show that RBD-binding mono-DARPin molecule #3 inhibits SARS-CoV-2 through receptor functional mimicry, facilitating fusogenic conformational rearrangements of the spike protein. This mechanism of inhibition was also observed for a SARS-CoV neutralizing antibody, S230[17], and more recently for a SARS-CoV-2 neutralizing antibody, C105[19].

Following a 15 second incubation with the S1-NTD-binding mono-DARPin molecule #9, 2D classification already revealed clear additional density bound to the spike NTD (Supplementary Figure 3a-b). Subsequent 3D classification revealed that most of the DARPin-bound spikes were in the closed conformation, and 19% had one RBD in open conformation (Supplementary Figure 3c). 3D refinement of the fully closed class produced an 8.8 Å global resolution map (supplementary Figure 3d), sufficient to dock and assign the pose of the bound DARPin molecule (Figure 2c). This mono-DARPin molecule binds to the most distal region of the NTD, which is not resolved in the majority of available spike structures[13,20]. However, several spike structures with nearly completely modelled NTDs were recently

bioRxiv preprint doi: https://doi.org/10.1101/2020.08.25.256339; this version posted August 26, 2020. The copyright holder for this preprint (which was not certified by peer review) is the author/funder, who has granted bioRxiv a license to display the preprint in perpetuity. It is made available under aCC-BY-NC-ND 4.0 International license.

reported[21,22]. The better resolved NTD loops in these structures allowed us to further narrow down the DARPin epitope, indicating that the concave binding surface is ideally situated to interact with the N5 loop, encompassing residues 246-258[23] (Figure 2d). A recently described monoclonal antibody, 4A8[23], also targets the NTD, involving an extensive hydrophilic interaction network with the N3 loop and, to a lesser extent, the N5 loop. In contrast, molecular docking experiments suggest mono-DARPin molecule #9 interacts with the NTD primarily through hydrophobic interactions with N5 loop residues 248-252 (Supplementary Figure 3e), with an interface area of ~600 Å^2. Structural analysis of S ectodomains incubated with the S2 binder #10 did not reveal any unambiguous density for the bound mono-DARPin (data not shown). The low number of intact ectodomains present following incubation with mono-DARPin #10 suggests that the S2 binder compromises the structural integrity of spike.

Rational design of multi-DARPin molecules targeting SARS-CoV-2 spike

We aimed to increase virus neutralizing potency through molecular linkage of mono-DARPin molecules, using the 11 mono-specific DARPin molecules that were characterized in molecular detail (Table 1). A total of 31 multi-DARPin molecules were generated, each comprising 3 mono-DARPin molecules against various epitopes of the spike protein as well as two mono-DARPin molecules against human serum albumin (HSA), which has been shown to confer long half-life in animals and humans (Table 2). The assembly of these 5-domain multi-DARPin molecules was guided by the rationale to diversely cover different spike epitopes and the combinatorial learnings of the 192 randomly assembled tri-DARPin molecules, in order to come up with the most potent molecules as well as good development requirements such as stability and other biophysical properties. Each of the 31 multi-DARPin molecules contained at least one RBD-binding domain since preventing ACE2 receptor interaction is assumed to be the strongest point of interference with viral particles entering into the host cell. Some of the 31 multi-DARPin molecules were designed to contain several binding molecules to the same spike domain. Molecules containing only RBD-binding domains are called “multi-RBD” DARPin molecules whereas the remaining DARPin molecules are called “multi-mode” DARPin molecules, to indicate the combination of different modes of action of viral inhibition (i.e. inhibition of protease cleavage and cell fusion mechanisms, inhibition of conformational change, or inhibition of binding to human receptors such as ACE2). All 31 multi-DARPin molecules were also profiled for their biophysical properties and share the typical DARPin properties of high thermal stability (Table 2) and high soluble expression levels (data not shown). When comparing the affinities of the mono-DARPin molecules with the multi-DARPin molecules, it became apparent that the combination of several pM and nM mono-DARPin molecules (Supp. Figure 4) leads to affinities/avidities below the limit of quantification by surface plasmon resonance (data not shown). The viral neutralization potency of 22 of the 31 multi-DARPin molecules was assessed in two screening titration PsV NAs and IC_{50} values

bioRxiv preprint doi: https://doi.org/10.1101/2020.08.25.256339; this version posted August 26, 2020. The copyright holder for this preprint (which was not certified by peer review) is the author/funder, who has granted bioRxiv a license to display the preprint in perpetuity. It is made available under aCC-BY-NC-ND 4.0 International license.

spanning a range from 98-1267 pM were observed (the format learnings from the first screening batch already supported to discard 9 of the 31 initial candidates) (Table 2). It was observed in various viral assays (PsV NA and authentic SARS-CoV-2), that the IC_{50} values of the most potent multi-DARPin molecules were determined by the number of viral particles within the assay, indicating even higher potencies then identified in the screening assays. A confirming titration PsV NA assay, using very low viral particle numbers, was performed with the most promising 12 multi-DARPin molecules, which showed viral neutralization IC_{50} values even in the low pM range (Figure 3a). SARS-CoV-2 neutralization capacity for 19 of the 31 multi-DARPin molecules was confirmed using the authentic pathogenic strain, where cell protection of susceptible Vero E6 cells was observed at concentrations ranging from 16 pM to 100 pM, corresponding to 1.3 ng/ml to 8 ng/ml (Table 2).

For two multi-DARPin molecules, representative for the two different formats (i.e. Multi-RDB-DARPin-Candidate, MR-DC, and Multi-Mode-DARPin-Candidate, MM-DC), the assay with the infectious SARS-CoV-2 was performed in a better resolved titration range, resulting in IC_{50} values of 12 pM for MR-DC (1 ng/ml) and 80 pM for MM-DC (7 ng/ml), respectively (Figure 4). Those extremely high potencies are key for the use of any molecule in SARS-CoV-2 treatment especially also in a prophylactic setting where very low virus titers at infection initiation are expected.

Guided by cryoEM data, we generated structural models of the MR-DC and MM-DC molecules in contact with the spike protein using 3D molecular modeling tools (Figure 5). The length of the linker allows simultaneous binding the NTD and the RBD binding DARPin molecules, whereas half-life extension modules have sufficient space to bind HSA. Within the distance limited by the linker length, we identified a potential binding site for the S2 binder, suggesting that simultaneous binding of to the spike protein is feasible.

Robustness against viral escape of multi-DARPin molecules

Next, we assessed in a PsV NA the impact of several spike protein variants of the most abundant SARS-CoV-2 strains, including one carrying the frequently occurring D614G mutation. All strains were neutralized with high potency by the two representative multi-DARPin molecules, MR-DC and MM-DC (Table 3), indicating robustness against viral escape.

To simulate a potential loss of binding to the RBD domain, e.g. following the accumulation of several viral mutations, 10 nM soluble RBD protein (a concentration chosen well below the interaction affinity of human ACE2 and RBD, to not influence the assay performance, but high enough to fully block the RBD binding DARPin component) was co-incubated with multi-DARPin molecules and the mixture subsequently assessed for its inhibition potential in a pseudovirus neutralization assay. Whereas the multi-RBD DARPin molecule MR-DC displayed about a 30-fold inferior IC_{50} of about 4 nM (in the range

bioRxiv preprint doi: https://doi.org/10.1101/2020.08.25.256339; this version posted August 26, 2020. The copyright holder for this preprint (which was not certified by peer review) is the author/funder, who has granted bioRxiv a license to display the preprint in perpetuity. It is made available under aCC-BY-NC-ND 4.0 International license.

of soluble RBD added), the multi-mode DARPin MM-DC molecule almost fully maintained its potency, (Figure 3b).

High-density fermentation and concentration of multi-DARPin molecules

To assess the suitability for development of two representative multi-DARPin molecules (Multi-RDB-DARPin-Candidate, MR-DC and Multi-Mode-DARPin-Candidate, MM-DC), they were expressed in high-density fermentation and resulted in yields of 12-17 g/L. The resulting protein was purified and concentrated to estimate the potential to deliver a sub-cutaneous formulation: 120 mg/mL was reached without reaching limiting viscosity.

In vivo antiviral efficacy of a multi-DARPin in a SARS-CoV-2 hamster infection model

A hamster PD model was performed to study the potential of multi-DARPin molecules for preventing SARS-CoV-2 related disease, (Figure 6). Golden Syrian hamsters (6 females per group) were treated with a single intraperitoneal dose of one multi-DARPin molecule, MR-DC, using either 16 µg, 160 µg, 1600 µg, or with placebo, 24 h prior to intranasal infection with SARS-CoV-2. Readouts included observation of body weight, macroscopic assessment of lung lesions, virus titers, and histopathology. At the 1600 µg dose, the multi-DARPin molecule produced significant reduction of the viral titers in the lung (7). Furthermore, dose-dependent reductions in virus titers, macroscopically determined lung lesions and body weight loss were observed, indicating that both the 160 µg and the 1600 µg doses have anti-viral activity under the conditions of the hamster model. Sufficient exposure was independently confirmed in healthy Golden Syrian hamsters at 160 µg and 1600 µg (Figure 6c). Histopathology (Figure 7, Table 4) and viral titer ($TCID_{50}$ and qPCR) data confirmed that the 1600 µg dose had the strongest protective effects.

bioRxiv preprint doi: https://doi.org/10.1101/2020.08.25.256339; this version posted August 26, 2020. The copyright holder for this preprint (which was not certified by peer review) is the author/funder, who has granted bioRxiv a license to display the preprint in perpetuity. It is made available under aCC-BY-NC-ND 4.0 International license.

Discussion

Additional solutions to combat the COVID-19 pandemic are urgently needed. Next to vaccination approaches, monoclonal antibodies have led to a lot of promise, based on highly potent inhibitors and promising animal efficacy. However, due to the global scale of COVID-19, manufacturing is expected to become a major bottleneck to make medicines readily available to all individuals in need. Next to antibodies, a number of alternative molecules have been developed to complement and partially overcome drawbacks of antibodies. Here we set out to isolate DARPin molecules - one prominent alternative to antibodies[24] - that bind the SARS-CoV-2 spike protein. We tested a library of one trillion DARPin molecules and identified multiple DARPin molecules with different functionalities and binding specificities. By molecular linkage of individual DARPin molecules, we developed multi-DARPin molecules with picomolar neutralizing activity and demonstrated their protective efficacy against SARS-CoV-2 infection in a hamster model.

The most potent neutralizing DARPin molecules were found to target the receptor binding domain blocking the spike-ACE2 interaction. This finding is congruent with the identified epitopes of potent neutralizing antibodies obtained from COVID-19 patients[9,25-29]. Thus, the *in vitro* approach using DARPin molecules independently confirms that the ACE2 interaction site on the SARS2-CoV-2 spike protein is one of the most vulnerable epitope to block virus infection in cell culture.

The single chain binding domain nature of DARPin molecules facilitated the design of multivalent and multispecific DARPin molecules with greatly increased neutralization potency. Virus neutralization capacity increased a thousand times when three DARPin molecules were linked - relative to the individual modules - likely due to both improved binding to the trimeric spike proteins by increased avidity as well as targeting of multiple spike domains. A similar strategy with comparable outcome has been recently applied for nanobodies[30]. The observed neutralization capacity of the multi-DARPin moleculess in the low picomolar range is similar or even outcompetes the neutralizing capacity of monoclonal antibodies. The multi-DARPin molecules are expected to retain potency even if the spike protein of SARS-CoV-2 should mutate considerably in future, especially when multiple modes of action are addressed.

DARPin molecules[24] have shown good promise for both ophthalmology and oncology patients. Within oncology, MP0250 is the DARPin molecule[31] with most data available to date: MP0250 is a dual inhibitor of VEGF and HGF and is being developed for multiple myeloma in combination with small molecules. MP0250 shows a long systemic half-life of about 2 weeks, low immunogenicity potential, and has been given to individual patients for more than two years. Here, we demonstrate *in vivo* prophylactic protection from SARS-CoV-2 infection by a multi-DARPin in a hamster model. Also, the half-lives reported here appear comparable to the half-lives reported for monoclonal antibodies. Thus, the multi-DARPin molecules represent very attractive potential therapeutics for clinical studies.

bioRxiv preprint doi: https://doi.org/10.1101/2020.08.25.256339; this version posted August 26, 2020. The copyright holder for this preprint (which was not certified by peer review) is the author/funder, who has granted bioRxiv a license to display the preprint in perpetuity. It is made available under aCC-BY-NC-ND 4.0 International license.

Generally, DARPin molecules can be easily produced in bacterial expression systems at high yields allowing cost-effective and scalable production of antiviral biologicals at industrial quantities. Consequently, global access to this novel class of therapeutics may be highly additive to monoclonal antibody approaches and thus contribute to overcoming the COVID-19 pandemic. Our results show the potential of multi-DARPin molecules for the prevention or treatment of COVID-19.

We anticipate that the presented workflow for DARPin development can be used for any future emerging (corona)virus. We have proven that high affinity binding and potently neutralizing DARPin molecules can be developed in a matter of weeks, without the requirement of immunization of animals or access to patient materials. Such fast track development strategies of picomolar inhibitors are critical to raise preparedness level towards novel pandemic viruses.

Data availability

The EM density maps (unsharpened, sharpened, half maps and mask) will be deposited to the Electron Microscopy Data Bank. The mono-DARPin and multi-DARPin sequences, and atomic coordinates derived from molecular docking experiments, are available (by contacting the corresponding author) for research purposes only under an MTA, which allows the use of the data for non-commercial purposes but not their disclosure to third parties.

bioRxiv preprint doi: https://doi.org/10.1101/2020.08.25.256339; this version posted August 26, 2020. The copyright holder for this preprint (which was not certified by peer review) is the author/funder, who has granted bioRxiv a license to display the preprint in perpetuity. It is made available under aCC-BY-NC-ND 4.0 International license.

Acknowledgements

We would particularly like to thank those employees of Molecular Partners who are not included in the author list and are currently advancing the program towards the clinic. Additionally, we would like to thank our former board member, William Lee, and the Virology group at Gilead Sciences for their helpful input. The authors also thank Dr. Gert Zimmer for the gift of the recombinant VSV (Institute of Virology and Immunology (IVI), CH-3147 Mittelhäusern, Switzerland, Department of Infectious Diseases and Pathobiology, Vetsuisse Faculty, University of Bern, CH-3012 Bern, Switzerland). The expression plasmid for SARS-2 S was kindly provided by Dr. Giulia Torriani and Dr. Isabella Eckerle (Department of Medicine, University of Geneva, Switzerland).

SR & JM were supported by Swiss Federal Office for Civil Protection (Grants Nr. 353008564/Stm, 353008218/Stm, and 353008560/Stm to Olivier Engler and Stefan Kunz).

We would like to thank for the supply of the two 2019-nCoV strains: i) 2019-nCoV/IDF0372/2020 provided by the National Reference Centre for Respiratory Viruses hosted by Institut Pasteur (Paris, France) and headed by Dr. Sylvie van der Werf as well as the human sample from which strain 2019-nCoV/IDF0372/2020 was isolated, provided by Dr. X. Lescure and Pr. Y. Yazdanpanah from the Bichat Hospital.

D.L.H. is funded from by the European Union's Horizon 2020 research and innovation program under the Marie Skłodowska-Curie grant agreement (No 842333) and holds an EMBO non-stipendiary long-term Fellowship (ALTF 1172-2018).

Funding

All studies were funded by Molecular Partners AG, Switzerland.

Author contributions

M.W., S.R., D.L.H., V.C., C.R., S.F., A.Z., N.V., K.M.D., C.Z., M.A.H., L.d.W., K.J.S., F.J.M.v.K., O.E. , B.-J. B.: conceptualized and designed experiments; M.W., S.R., D.L.H., A.S., D.V., M.P., T.H., A.N., A.C., P.S., M.M., M.H., M.F., Y.K., I.S., C.I., T.L., S.M., C.H., D.S., A.B., A.L., T.V., G.S., K.P., M.S., J.M., S.Ry., H.L., C.W., W.L., I.D.: performed laboratory experiments; D.L.H., F.R.: performed computational work; M.W., S.R., D.L.H., H.K.B., S.L., S.F., F.J.M.v.K., O.E., B.-J. B., M.T.S., P.A. drafted the manuscript. S.L., D.S., M.T.S., P.A. acquired funding. All authors reviewed the manuscript.

Competing interests: Molecular Partners authors own performance share units and/or stock of the company. HKB owns stock of the company.

bioRxiv preprint doi: https://doi.org/10.1101/2020.08.25.256339; this version posted August 26, 2020. The copyright holder for this preprint (which was not certified by peer review) is the author/funder, who has granted bioRxiv a license to display the preprint in perpetuity. It is made available under aCC-BY-NC-ND 4.0 International license.

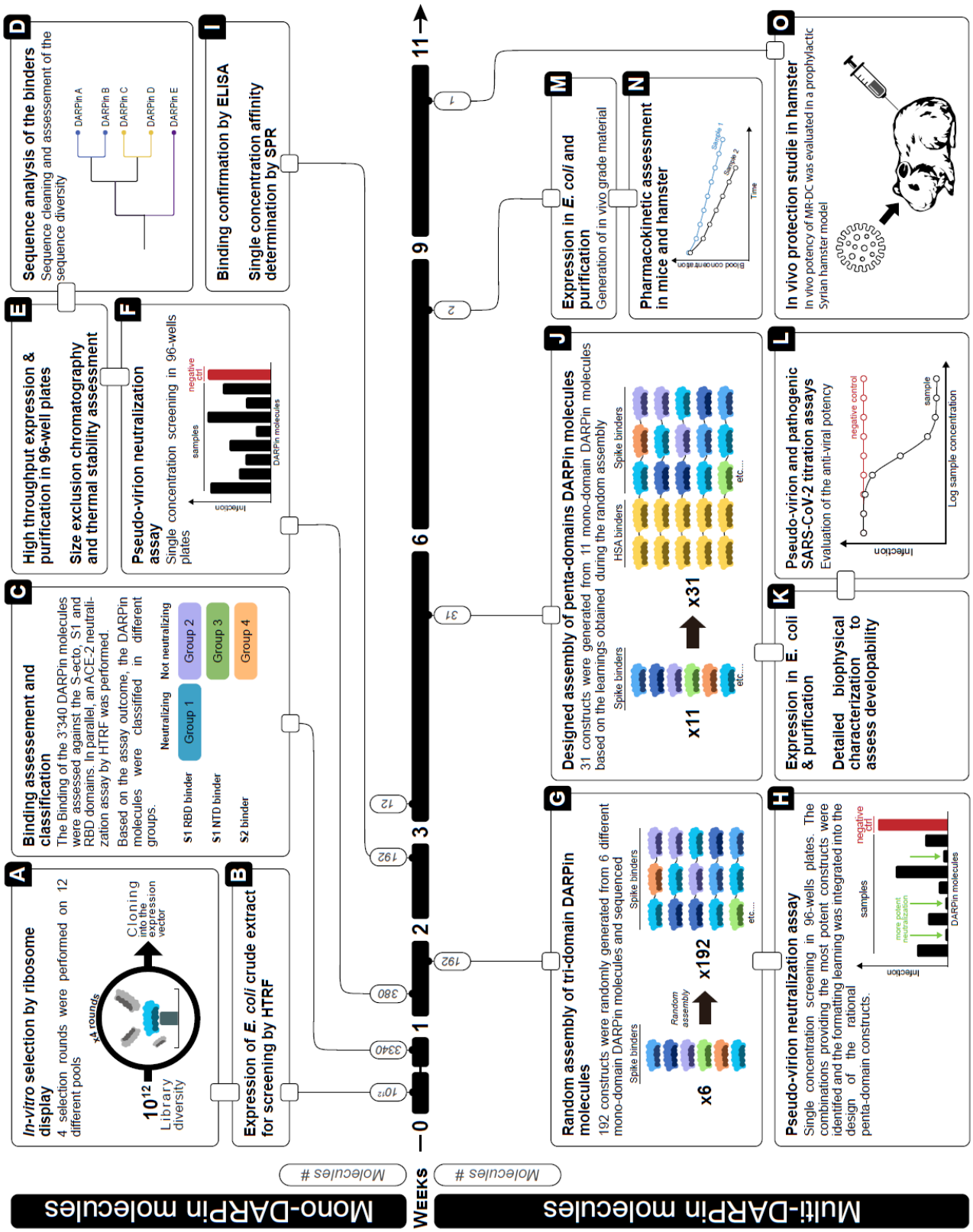

Figure 1: Process overview for the generation of anti-SARS-CoV-2 multi-DARPin molecules. Upper panel, generation and evaluation of mono-DARPin molecules. Lower panel, assembly and deep-characterization of multi-DARPin molecules.

5

bioRxiv preprint doi: https://doi.org/10.1101/2020.08.25.256339; this version posted August 26, 2020. The copyright holder for this preprint (which was not certified by peer review) is the author/funder, who has granted bioRxiv a license to display the preprint in perpetuity. It is made available under aCC-BY-NC-ND 4.0 International license.

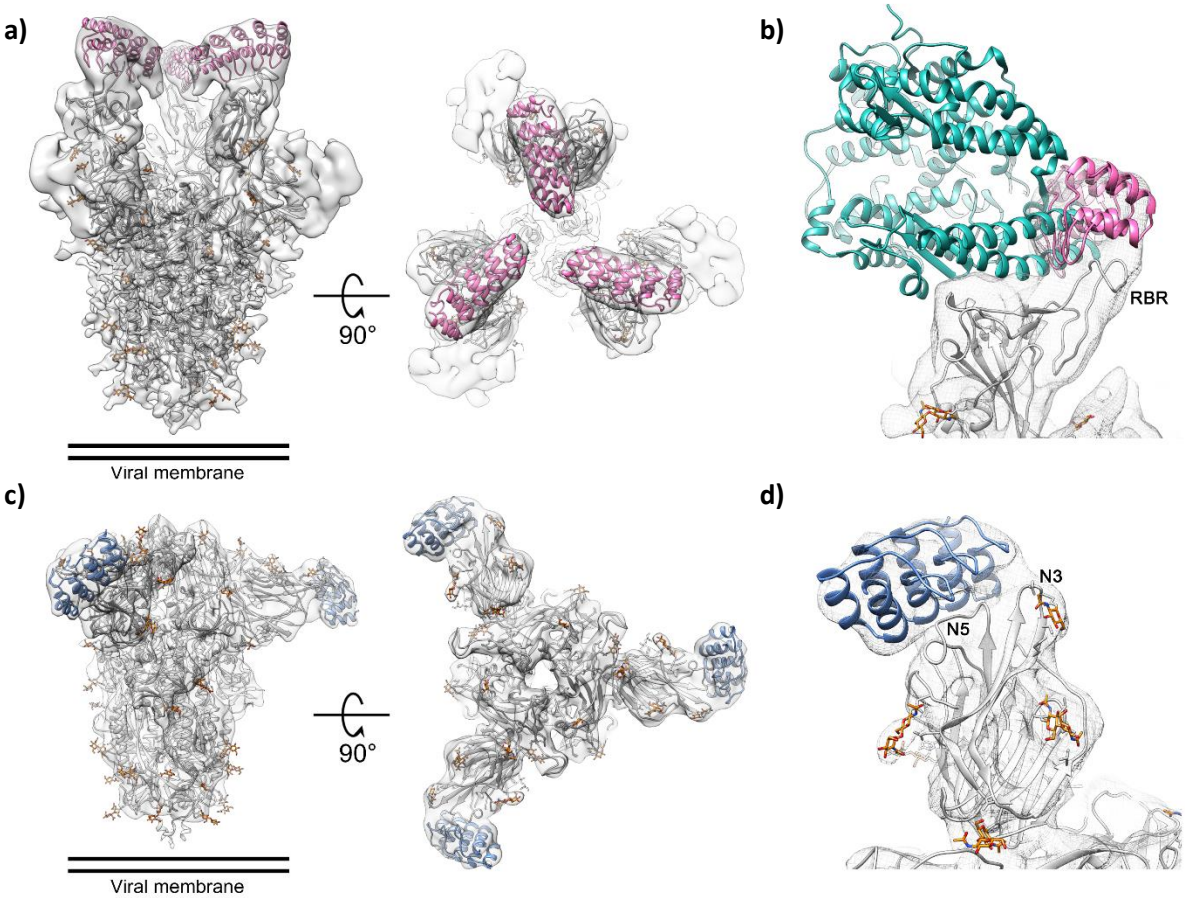

Figure 2: Cryo-EM analysis of mono-DARPin molecules. a) Cryo-EM density for the SARS-CoV-2 spike ectodomain in complex with the RBD targeting DARPin, shown as two orthogonal views. The atomic coordinates for the fitted fully open spike (PDB ID: 6XCN) and the DARPin homology model are overlaid and colored grey and pink, respectively. b) Zoomed in view of the DARPin bound RBD with the cryo-EM density shown as a grey mesh. The atomic coordinates of the RBD bound ACE2 (PDB ID: 6M0J), colored green, is superimposed. c) Cryo-EM density for the SARS-CoV-2 spike ectodomain in complex with the NTD targeting DARPin, shown as two orthogonal views. The atomic coordinates for the fitted fully closed spike (PDB ID: 6ZGE) and the DARPin homology model are overlaid and colored grey and blue, respectively. d) Zoomed in view of the DARPin bound NTD with the cryo-EM density shown as a grey mesh. The N3 and N5 loops are labelled and glycans are shown in stick representation and colored orange.

bioRxiv preprint doi: https://doi.org/10.1101/2020.08.25.256339; this version posted August 26, 2020. The copyright holder for this preprint (which was not certified by peer review) is the author/funder, who has granted bioRxiv a license to display the preprint in perpetuity. It is made available under aCC-BY-NC-ND 4.0 International license.

a)

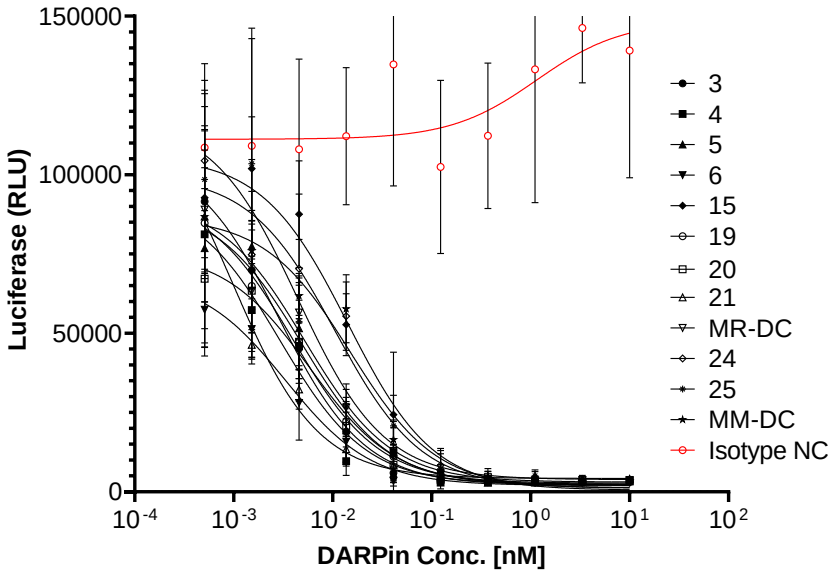

Name	IC_{50} [pM]
3	2.9
4	2.9
5	4.9
6	3.4
15	14.2
19	4.0
20	5.9
21	0.96
MR-DC	5.2
24	10.6
25	4.4
MM-DC	15.2

b)

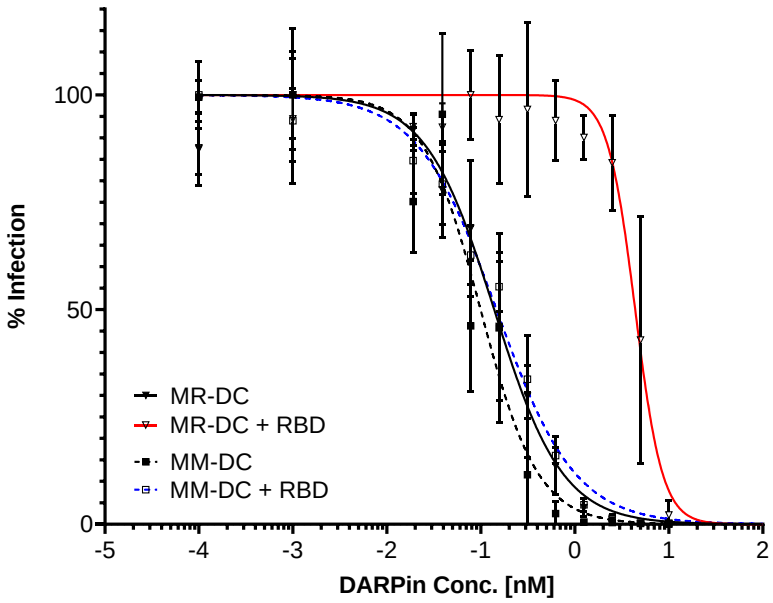

Figure 3: a) Titration of 12 multi-DARPin molecules (black lines) in a PsV-NA assay at very low viral titers for determination of VSV-SARS-CoV-2 neutralization. Multi-DARPin molecule negative control (solid red line). b) Evaluation of potency loss for candidates MR-DC and MM-DC when blocking the RBD-binding mono-DARPin molecule with soluble RBD (Fc-dimerized). MM-DC (dashed black line), MM-DC with blocked RBD-binding entity (dashed blue line), MR-DC (solid black line), MR-DC with blocked RBD-binding entity (solid red line).

bioRxiv preprint doi: https://doi.org/10.1101/2020.08.25.256339; this version posted August 26, 2020. The copyright holder for this preprint (which was not certified by peer review) is the author/funder, who has granted bioRxiv a license to display the preprint in perpetuity. It is made available under aCC-BY-NC-ND 4.0 International license.

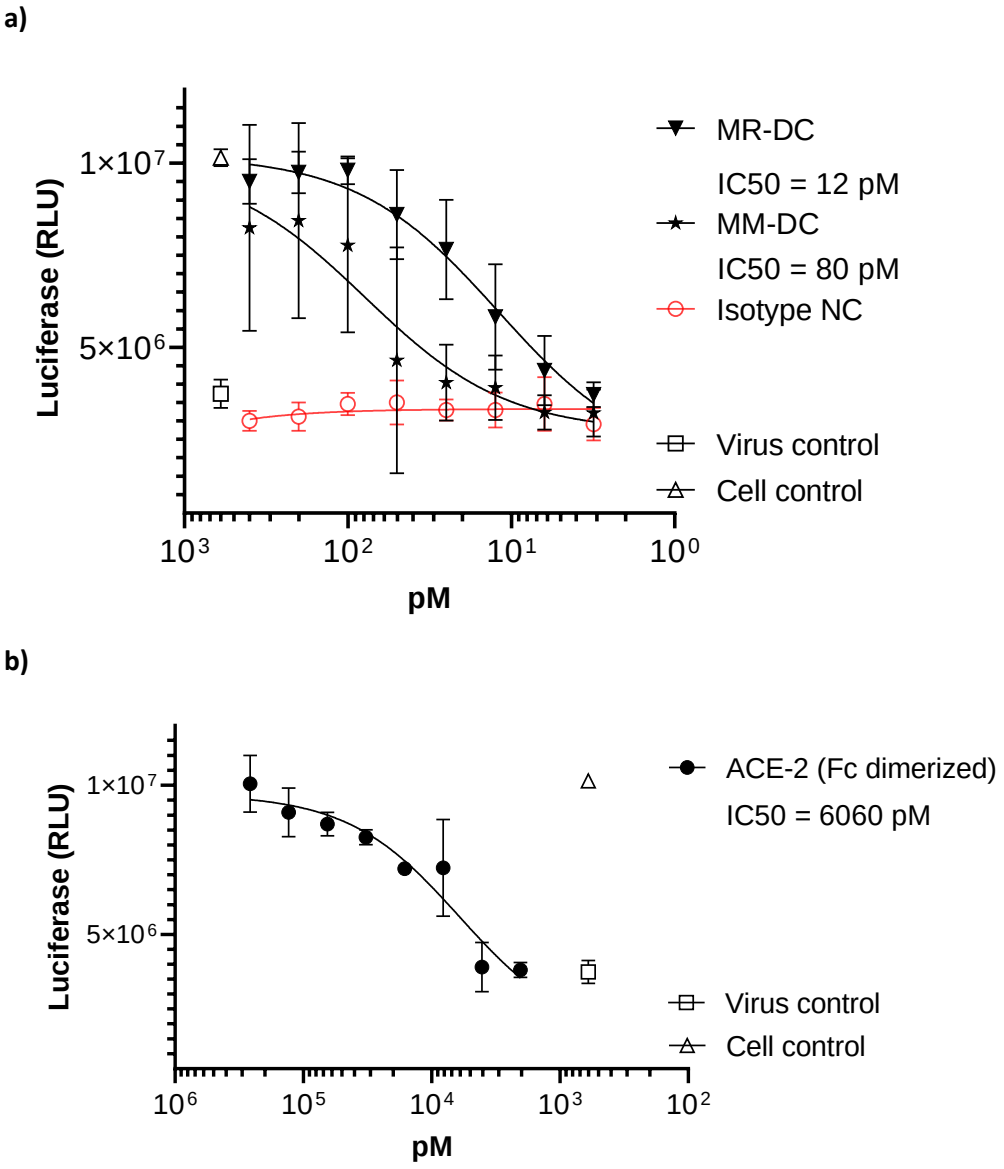

Figure 4: Evaluation of Cytopathic Effect (CPE) for infection of susceptible Vero E6 cells when incubated with infectious SARS-CoV-2 (Cell Titer Glo Assay). a) Titration data for the two representative multi-DARPin molecules MR-DC (triangle down) and the MM-DC (stars) respectively a multi-DARPin negative control (hollow circles); b) As a positive control Fc-dimerized human ACE2 was employed in the same assay (full circles).

bioRxiv preprint doi: https://doi.org/10.1101/2020.08.25.256339; this version posted August 26, 2020. The copyright holder for this preprint (which was not certified by peer review) is the author/funder, who has granted bioRxiv a license to display the preprint in perpetuity. It is made available under aCC-BY-NC-ND 4.0 International license.

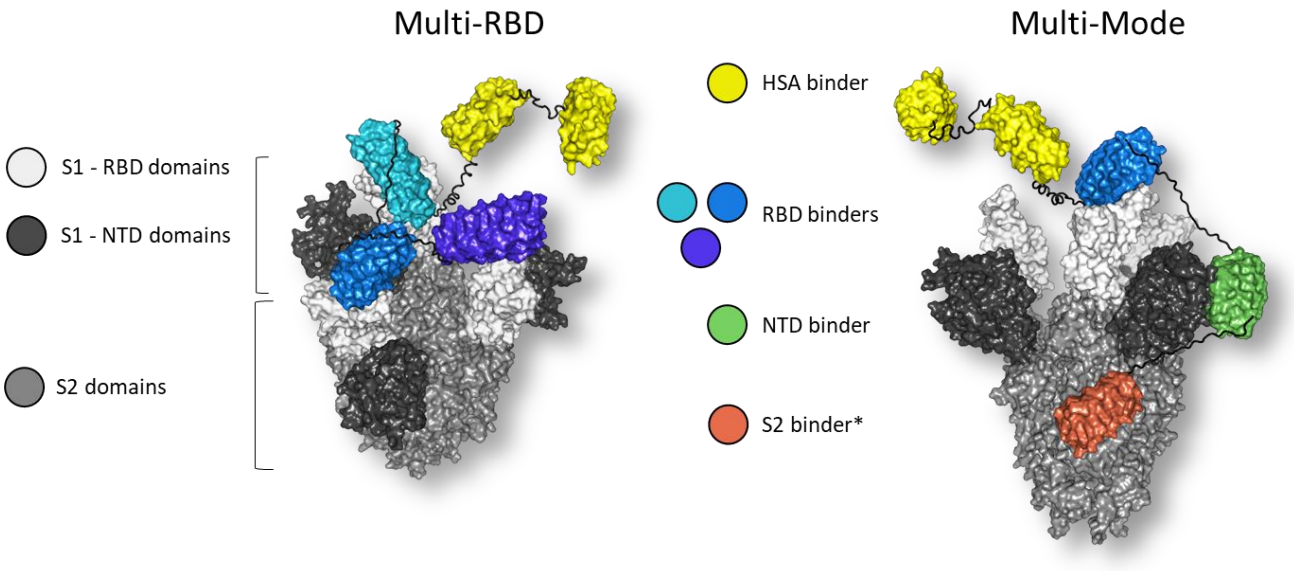

Figure 5. Molecular model[32] of multi-DARPin molecule MM-DC (right), consisting of five DARPin domains (yellow: HSA-binding domains, blue: RBD-binding domain, green: NTD-binding domain, orange: S2-binding domain) bound to the spike ectodomain. Linkers are shown in black. Molecular model[32] of MR-DC (left) consisting of five DARPin domains (yellow: HSA-binding domains, shades of blue: RBD-binding domains) bound to the RBDs (white) of the spike ectodomain (grey). Linkers are shown in black.

Position of RBD and NTD binders guided by Cryo-EM data (Figure 2) - *Positioning on spike protein remains uncertain for the S2 binder and is guided by manual docking and not based on Cryo-EM data.

bioRxiv preprint doi: https://doi.org/10.1101/2020.08.25.256339; this version posted August 26, 2020. The copyright holder for this preprint (which was not certified by peer review) is the author/funder, who has granted bioRxiv a license to display the preprint in perpetuity. It is made available under aCC-BY-NC-ND 4.0 International license.

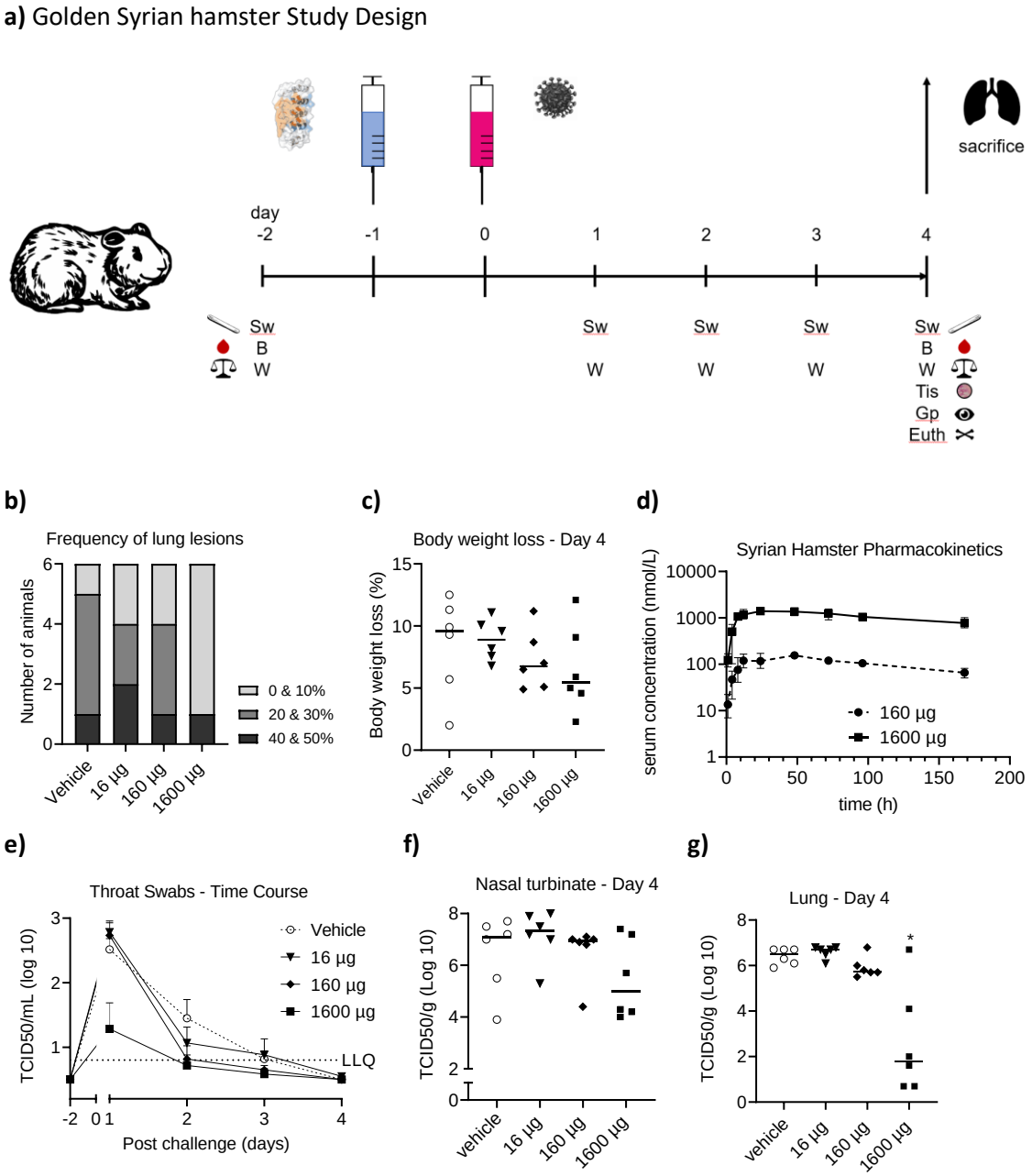

Figure 6. In-vivo efficacy of MR-DC in treating SARS-CoV-2 infection in a preventive Golden Syrian hamster model. A) study design: six animals were used per dose group. Generally high variations were observed in control and treatment groups. At Day -2, body weight (W) was measured, blood (B) was taken, and the first throat swab (Sw) performed. Animals were euthanized on Day 4 and tissue (Tis) were taken and gross pathology (Gp) was performed. MR-DC exhibits (b) a trend to dose-dependent reduction of the frequency of macroscopically observed lung lesions (detailed pathology data is listed in Table 3), and (c) a trend to dose-dependent reduction of body-weight loss at day 4. d) Pharmacokinetic exposure at 160 µg and 1600 µg (e-g) Virus titers post challenge for throat swabs (e), nasal turbinate (f) and significant reduction of viral loads in the lung at 1600 µg with a trend to dose-dependent reduction of viral loads (g).

bioRxiv preprint doi: https://doi.org/10.1101/2020.08.25.256339; this version posted August 26, 2020. The copyright holder for this preprint (which was not certified by peer review) is the author/funder, who has granted bioRxiv a license to display the preprint in perpetuity. It is made available under aCC-BY-NC-ND 4.0 International license.

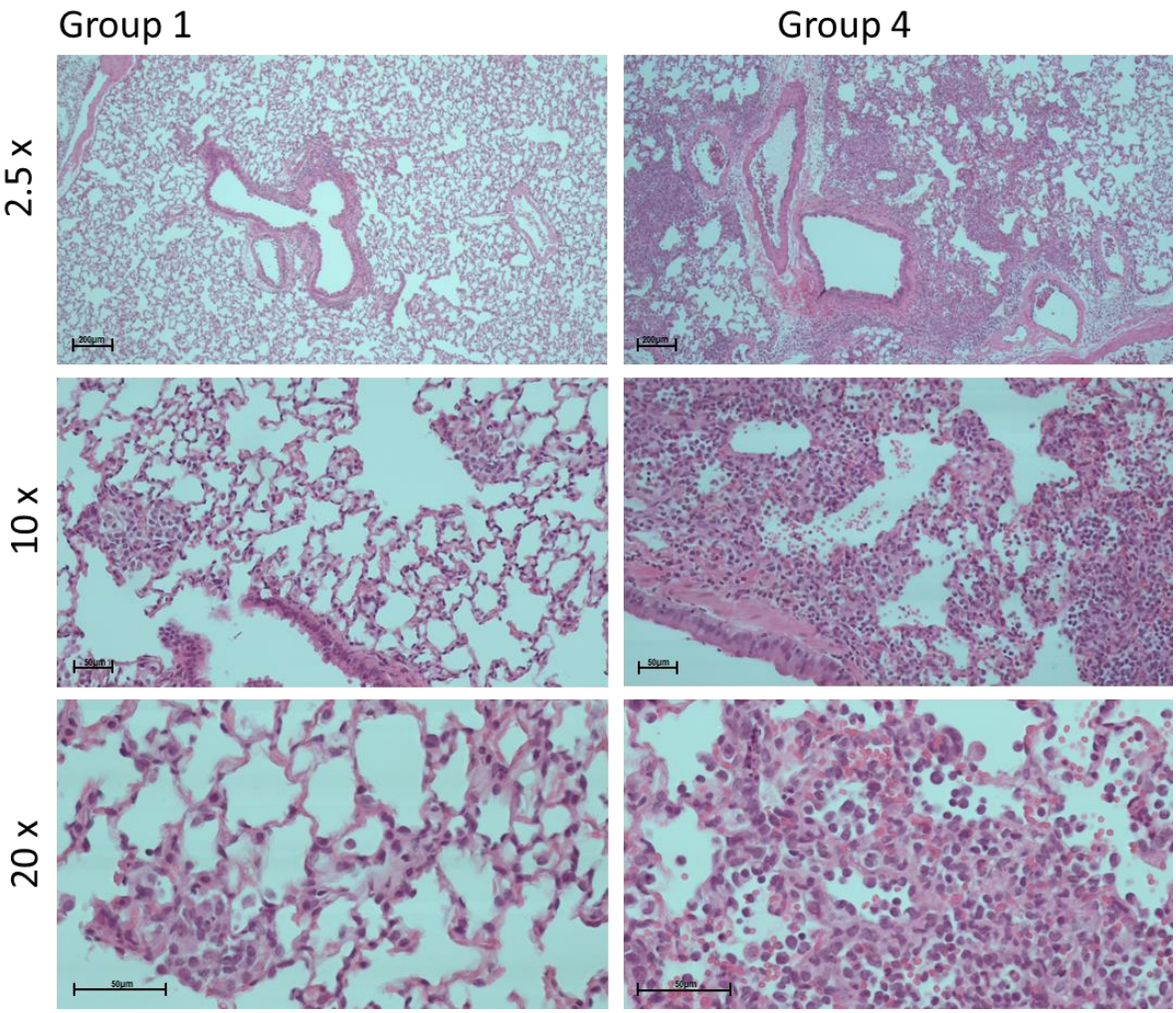

Figure 7: Representative histopathology microscopic pictures of hamster lung tissue taken at day 4. Left panel, hamster lung tissue of an animal treated with 1600 µg MR-DC (group 1); right panel, inflamed lung tissue showing mild hemorrhage, alveolar wall thickening and proliferation of pneumocytes of an animal which received the placebo injection (group 4)

bioRxiv preprint doi: https://doi.org/10.1101/2020.08.25.256339; this version posted August 26, 2020. The copyright holder for this preprint (which was not certified by peer review) is the author/funder, who has granted bioRxiv a license to display the preprint in perpetuity. It is made available under aCC-BY-NC-ND 4.0 International license.

Table 1: List of spike protein-binding mono-DARPin molecules and their properties

Name	*Binding domain*	*Viral Neutralization*	*PsV NA – Single Conc. Screenings* [10^{-9} M]	*K_D [10^{-9} M]*	*SEC Profile*	*Tm [°C]*	*Size [kDa]*
1	RBD	Neutralizing	1-10	0.258*	Monomer	*>65*	*~14*
2	RBD	Neutralizing	1-10	0.220**	Monomer	>85	*~17*
3	RBD	Neutralizing	1-10	0.030*	Monomer	>85	*~17*
4	RBD	Neutralizing	1-10	0.390**	Monomer	>85	*~17*
5	RBD	Neutralizing	1-10	0.090*	Monomer	>85	*~17*
6	RBD	Neutralizing	1-10	0.080*	Monomer	>85	*~17*
7	RBD	Non-neutralizing	no neutralization	8.10**	Monomer	>80	*~14*
8	RBD	Non-neutralizing	no neutralization	10.0**	Monomer	n.a.	*~14*
9	NTD	Non-neutralizing	no neutralization	1.24*	Monomer	n.a.	*~14*
10	S2	Partial Neutralization	10-100	0.785*	Monomer	>85	*~14*
11	S2	Partial Neutralization	10-100	n.a.	Monomer	>85	*~17*

* Multi concentration SPR measurement

** Single concentration SPR measurement

n.a.: not applicable

bioRxiv preprint doi: https://doi.org/10.1101/2020.08.25.256339; this version posted August 26, 2020. The copyright holder for this preprint (which was not certified by peer review) is the author/funder, who has granted bioRxiv a license to display the preprint in perpetuity. It is made available under aCC-BY-NC-ND 4.0 International license.

Table 2. Properties of SARS-CoV-2 inhibiting drug candidates

Construct Name	5D-Multi-DARPin					IC$_{50}$ PsV NA (*Screening setting - Assay 1)	IC$_{50}$ PsV NA (*Screening setting - Assay 2)	Cytopathic effect Live Virus**	SEC Profile	Tm [°C] (CD)
	1	2	3	4	5	[10^{-9} M]	[10^{-9} M]	[10^{-9} M]		
MR-DC	**H**	**H**	**6**	**3**	**5**		**0.1988**	**< 0.025**	**Monomeric**	**>85**
MM-DC	**H**	**H**	**5**	**9**	**10**	**0.2278**		**< 0.100**	**Monomeric**	**>85**
3	H	H	6	1	3	0.1195		< 0.080	Monomeric	>80
4	H	H	4	2	1		0.2606	< 0.080	Monomeric	>75
5	H	H	4	6	3		0.2806	n.a	Monomeric	>85
6	H	H	6	3	6	0.1247		< 0.016	Monomeric	>85
7	H	H	7	3	6	0.2407		< 0.016	Monomeric	>80
8	H	H	8	4	1	0.2377		< 0.080	Monomeric	>85
9	H	H	3	6	7		n.a.***	n.a	Monomeric	>85
10	H	H	4	1	8	0.2632		< 0.050	Monomeric	>85
11	H	H	3	6	9	0.2638		< 0.080	Monomeric	>85
12	H	H	9	3	6	0.2792		< 0.080	Monomeric	>80
13	H	H	1	6	9	0.4175		< 0.080	Monomeric	>75
14	H	H	9	6	1	0.4756		< 0.080	Monomeric	>80
15	H	H	6	9	10	0.09803		< 0.080	Monomeric	>80
16	H	H	3	9	11	1.267		< 0.800	Monomeric	>85
17	H	H	10	9	6	0.1471		< 0.050	Monomeric	>85
18	H	H	11	9	3	0.6927		n.a	Monomeric	>80
19	H	H	5	1	3		0.3862	n.a	Monomeric	>80
20	H	H	1	2	5		0.3538	< 0.080	Monomeric	>80
21	H	H	3	5	6		0.2557	< 0.080	Monomeric	>85
22	H	H	7	3	5		n.a.***	n.a	Monomeric	>85
23	H	H	8	5	6		n.a.***	n.a	Monomeric	n.d.
24	H	H	6	10	11		0.2013	< 0.080	Monomeric	>85
25	H	H	3	10	10		0.1408	< 0.016	Monomeric	>80
26	H	H	5	6	9		n.a.***	n.a	Monomeric	n.d.
27	H	H	9	3	5		n.a.***	n.a	Monomeric	n.d.
28	H	H	9	6	5		n.a.***	n.a	Monomeric	n.d.
29	H	H	6	9	11		n.a.***	n.a	Monomeric	n.d.
30	H	H	10	9	5		n.a.***	n.a	Monomeric	n.d.
31	H	H	11	9	6		n.a.***	n.a	Monomeric	n.d.

H = HSA-Binding DARPin; n.a.: not applicable

* Higher viral titers used compared to illustrated titration curves, which leads to higher IC$_{50}$ values

** Titration assays for evaluation of cytopathic effect (CPE) by crystal violet staining

*** Format not pursued due to insights of the first PsV NA screening assay

bioRxiv preprint doi: https://doi.org/10.1101/2020.08.25.256339; this version posted August 26, 2020. The copyright holder for this preprint (which was not certified by peer review) is the author/funder, who has granted bioRxiv a license to display the preprint in perpetuity. It is made available under aCC-BY-NC-ND 4.0 International license.

Table 3. Neutralization potency (IC_{50}, [10^{-12}M]) for multi-DARPin molecules MR-DC and MM-DC for SARS-CoV-2 spike protein variants, frequently observed in sequencing data of globally appearing serotypes, were evaluated by PsV NA.

	wt	G476S	V483A	D614G	D614G x Q675H
MR-DC	16.53	27.08	27.48	11.77	12.11
MM-DC	5.48	14.46	32.40	4.64	22.44

bioRxiv preprint doi: https://doi.org/10.1101/2020.08.25.256339; this version posted August 26, 2020. The copyright holder for this preprint (which was not certified by peer review) is the author/funder, who has granted bioRxiv a license to display the preprint in perpetuity. It is made available under aCC-BY-NC-ND 4.0 International license.

Table 4. Histopathology results of the hamster study

Animal number	Group number	Compound	Dose	Extent of alveolitis/alveolar damage	Severity of alveolitis	SUM of extent + severity	Severity of bronchitis	Severity of bronchiolitis
1	1	MR-DC	1600 µg	1	1	2	2	1
2				0	0	0	1	1
3				1	2	3	3	1
4				1	1	2	3	1
5				1	1	2	2	1
6				0	0	0	1	1
7	2	MR-DC	160 µg	1	3	4	3	2
8				2	3	5	3	3
9				2	3	5	3	3
10				2	3	5	3	3
11				2	3	5	2	3
12				2	3	5	3	3
13	3	MR-DC	16 µg	2	3	5	3	3
14				2	3	5	3	3
15				3	3	6	3	3
16				2	3	5	3	3
17				1	3	4	3	2
18				3	3	6	3	3
19	4	Placebo	N/A	2	3	5	3	3
20				2	3	5	3	3
21				2	3	5	3	3
22				2	3	5	3	3
23				2	3	5	3	3
24				2	3	5	3	3

Animal number	Group number	Compound	Dose	Alveolar edema presence	Alveolar hemorrhage presence	Type II pneumocyte hyperplasia presence
1	1	MR-DC	1600 µg	no	no	no
2				no	no	no
3				no	no	yes
4				no	no	yes
5				no	no	yes
6				no	no	no
7	2	MR-DC	160 µg	yes	yes	yes
8				yes	yes	yes
9				yes	yes	yes
10				yes	yes	yes
11				yes	yes	yes
12				yes	yes	yes
13	3	MR-DC	16 µg	yes	yes	yes
14				yes	yes	yes
15				yes	yes	yes
16				yes	yes	yes
17				yes	yes	yes
18				yes	yes	yes
19	4	Placebo	N/A	yes	yes	yes
20				yes	yes	yes
21				yes	yes	yes
22				yes	yes	yes
23				yes	yes	yes
24				yes	yes	yes

bioRxiv preprint doi: https://doi.org/10.1101/2020.08.25.256339; this version posted August 26, 2020. The copyright holder for this preprint (which was not certified by peer review) is the author/funder, who has granted bioRxiv a license to display the preprint in perpetuity. It is made available under aCC-BY-NC-ND 4.0 International license.

Materials and Methods

SARS-CoV-2 spike proteins variants used

Proteins used for selections comprised SARS-CoV-2 S protein ectodomain (SARS2-Secto-d72-GCN4-Streptag; University of Utrecht), SARS-CoV-2 S protein (S1+S2 ECT, His-tag; Sinobiological 40589-V08B1), Bio-COVID-19_S1 protein_His_Avitag (Acro Biosystems), SARS2-S1-Flag-3Streptag (University of Utrecht), COVID-19_S_protein_RBD_Fc (Acro Biosystems), and SARS2-S1B-2Streptag (University of Utrecht). Proteins were biotinylated using standard methods.

Selection of SARS-CoV-2 spike protein-specific DARPin molecules by ribosome display

DARPin libraries[6] (N2C and N3C) were used in ribosome display selections[14,15] against the SARS-CoV-2 spike protein fragments. Four selection rounds were performed per target and library using decreasing target concentrations and increasing washing stringency to increase selection pressure from round 1 to round 4. The number of reverse transcription (RT)-PCR cycles after each selection round was continuously reduced, adjusting to the yield due to enrichment of binders. The 12 resulting pools were then subjected to a binder screening.

Screening of mono-DARPin molecules

Mono-DARPin molecules specifically binding to the S1-RBD, S1-NTD and S2 domains of the spike protein of SARS-CoV-2 in solution were identified by a homogeneous time resolved fluorescence (HTRF) assay using crude extracts of DARPin-expressing *Escherichia coli* (*E. coli*) cells using standard protocols. Briefly, DARPin clones selected by ribosome display were cloned into a derivative of the pQE30 (Qiagen) expression vector, *E. coli* XL1-Blue (Stratagene) was transformed and plated on LB-agar (containing 1% glucose and 50 µg/ml ampicillin) and then incubated overnight at 37°C. Single colonies were picked into individual wells of 96 well plates containing 165 µl growth medium (LB containing 1% glucose and 50 µg/ml ampicillin) and incubated overnight at 37°C, shaking at 800 rpm. 150 µl of fresh LB medium containing 50 µg/ml ampicillin was inoculated with 8.5 µl of the overnight culture in a fresh 96-deep-well plate. After incubation for 120 min at 37°C and 850 rpm, expression was induced with IPTG (0.5 mM final concentration) and continued for 6 h. Cells were harvested by centrifugation of the 96-deep-well plates, supernatant was discarded, and the pellets were frozen at -20°C overnight before resuspension in 8.5 µl B-PERII (Thermo Scientific) and incubation for 1 h at room temperature with shaking (600 rpm). Then, 160 µl PBS was added and cell debris was removed by centrifugation (3220 g for 15 min). The extract of each lysed clone was applied as a 1:200 dilution (final concentration) in PBSTB (PBS supplemented with 0.1% Tween 20® and 0.2% (w/v) BSA, pH 7.4) together with 20 nM (final concentration) biotinylated spike protein domain, 1:400 (final concentration) of anti-6His-D2 HTRF antibody – FRET acceptor conjugate (Cisbio) and 1:400 (final

bioRxiv preprint doi: https://doi.org/10.1101/2020.08.25.256339; this version posted August 26, 2020. The copyright holder for this preprint (which was not certified by peer review) is the author/funder, who has granted bioRxiv a license to display the preprint in perpetuity. It is made available under aCC-BY-NC-ND 4.0 International license.

concentration) of anti-strep-Tb antibody FRET donor conjugate (Cisbio, France) to a well of a 384-well plate and incubated for 120 min at 4°C. The HTRF was read-out on a Tecan M1000 using a 340 nm excitation wavelength and a 620±10 nm emission filter for background fluorescence detection and a 665±10 nm emission filter to detect the fluorescence signal for specific binding. The extract of each lysed clone was tested for binding to the biotinylated spike protein domains, in order to assess specific binding to the spike protein.

Cloning of multi-DARPin molecules

Multi-DARPin molecules were prepared using Gibson assembly as described[33]. The individual domains are linked with proline-threonine-rich polypeptide linkers[33].

DAPRin protein production and characterization

DARPin molecules were expressed in *E. coli* and purified as described[33]. Characterization of mono-DARPin molecules included SDS-PAGE (not shown), size exclusion chromatography, surface plasmon resonance, SARS-CoV-2 pseudotype virus inhibition assay, as well as live virus inhibition assay. Characterization of multi-DARPin molecules included SDS-PAGE (fully intact size without degradation; not shown), mass spectrometry (expected molecular weight; not shown), size exclusion chromatography coupled to static light scattering, circular dichroism, storage stability (stable at 60°C for 1 week; data not shown), serum stability (stable at 37°C in serum for one week; data not shown), surface plasmon resonance, SARS-CoV-2 pseudotype virus inhibition assay, live virus inhibition assay, hamster pharmacokinetic analysis, and hamster efficacy model.

Circular dichroism of DARPin molecules

Circular dichroism measurement was performed with a Jasco J-815 using a 1 cm pathlength cuvette (Hellma) with the monitor sensor inserted in the cuvette. The MRE at 222 nm was followed over a temperature ramp from 20°C to 90°C (heating and cooling). Spectra from 190-250 nm were taken before and after the variable temperature measurement at 20°C. The protein was measured at 0.25 μM in PBS.

Surface plasmon resonance affinity determination of DARPin molecules

SPR assays were used to determine the binding affinity of mono-DARPin as well as multi-DARPin molecules to the spike protein of SARS-CoV-2. All SPR data were generated using a Bio-Rad ProteOn XPR36 instrument with PBS-T (0.005% Tween20) as running buffer. A new neutravidin sensor chip (NLC) was air-initialized and conditioned according to Bio-Rad manual.

bioRxiv preprint doi: https://doi.org/10.1101/2020.08.25.256339; this version posted August 26, 2020. The copyright holder for this preprint (which was not certified by peer review) is the author/funder, who has granted bioRxiv a license to display the preprint in perpetuity. It is made available under aCC-BY-NC-ND 4.0 International license.

Mono-DARPin molecules: Chemically biotinylated (via lysines) SARS-CoV-2 spike protein 20 (Sino Biologics) was captured to ~3400 RUs (30 µg/ml, 30 µl/min, 300 s). Two buffer injections (100 µl/min, 60 s) followed by two 12.5 mM NaOH regeneration steps (100 µl/min, 18 s) were applied before the first injections. Mono-domain DARPin proteins were injected (at 50/16.7/5.6/1.9/0.6 nM) for 180 s at 100 µl/min for association and dissociation was recorded for 3600 s (at 100 µl/min). The ligand was regenerated with a 12.5 mM NaOH pulse (100 µl/min, 18 s). The data was double referenced against the empty surface and a buffer injection and fitted according to the 1:1 Langmuir model.

Multi-DARPin molecules: Chemically biotinylated (via lysines) COVID-19_S_protein_RBD_Fc (Acro Biosystems) was captured to ~1000 RUs (775 ng/ml, 30 µl/min, 300 s). Two buffer injections (100 µl/min, 60s) followed by two 12.5 mM NaOH regeneration steps (100 µl/min, 18s) were applied before the first injections. One single concentration of 25 nM of each multi- domain drug candidate was injected for 180 s at 100 µl/min for association and dissociation was recorded for 36'000 s (at 100 µl/min). The data was double referenced against the empty surface and a buffer injection. Due to avidity gain, no significant dissociation could be recorded during the measured time.

Cells and viruses

Vero E6 cells (African green monkey kidney cells, ATCC® CRL1586™) purchased from ATCC (Manassas, VA 20110 USA) were passaged in cell culture medium DMEM (FG0445) containing 10% FBS and supplements (2mM L-Glutamine, Non-essential amino acids and 100 U/ml Penicillin 100 µg/ml Streptomycin and HEPES, all from Biochrom, Berlin, Germany) at 37°C with CO2. SARS-CoV-2 (2019-nCoV/IDF0372/2020) kindly provided by Dr. Sylvie van der Werf from the National Reference Centre for Respiratory Viruses hosted by Institut Pasteur (Paris, France) was propagated in Vero E6 cells in MEM containing 2% FBS and supplements (2%-FBS-MEM) at 37°C and 5% CO_2.

Virus neutralization capacity of mono-DARPin and multi-DARPin molecules was determined for 100 $TCID_{50}$ SARS-CoV-2 by crystal violet staining of protected cells. DARPin molecules were serially diluted from 50 nM to 3.2 pM (in triplicates) in 100 µl cell culture medium (2%-FBS-MEM) enriched with 10 µM human serum albumin (HSA, CSL Behring, Switzerland) (2%-FBS-MEM + HSA) in 96 well plates. The diluted DARPin candidates were exposed to 100 $TCID_{50}$ SARS-CoV-2 (10^4 $TCID_{50}$/ml) in 100 µl 2%-FBS-MEM + HSA. DARPin/virus mixtures (200 µl) were transferred onto 80% confluent Vero E6 cells. The controls consisted of Vero E6 cells exposed to DARPin molecules only, to determine unspecific effects of the DARPin molecules, of cells exposed to virus suspension only to determine maximal cytopathic effect and of cells incubated with medium only, to determine baseline state of cells. The plates were incubated for 3 days at 37°C and the cytopathic effect determined by staining with 100 µl/well crystal violet solution (spatula tip (~4 mg) crystal violet powder (Sigma Aldrich) solved in 30 ml 37% formalin and 120 ml PBS (Sigma Aldrich)) for 10 min and washing plates with PBS (Sigma Aldrich). Wells were

bioRxiv preprint doi: https://doi.org/10.1101/2020.08.25.256339; this version posted August 26, 2020. The copyright holder for this preprint (which was not certified by peer review) is the author/funder, who has granted bioRxiv a license to display the preprint in perpetuity. It is made available under aCC-BY-NC-ND 4.0 International license.

visually evaluated for complete protection indicated by intact blue/violet cell layer or partial protection in case of >50% intact cell layer.

The effect of neutralization capacity of MultiDARPin was evaluated by exposing serial dilutions of the DARPin candidates to increasing titers of SARS-CoV-2 and determining cell protection by CellTiter-Glo assay (Promega, Madison, USA). Serial dilution of DARPin candidates were prepared in 96 well plates in 100 µl cell culture medium (2%-FBS-MEM + HSA) mixed with 100 µl virus suspension of 10^4 $TCID_{50}$/ml SARS-CoV-2 and incubated for 1 h at 37°C and 5% CO_2. DARPin/virus mixtures (200 µl) were transferred onto 80% confluent Vero E6 cells and plates incubated at 37°C for 3 days. Cell viability was determined by removing 100 µl supernatant from all wells and adding 100 µl CellTiter-Glo reagent as described in the manufacturers protocol (CellTiter-Glo® Luminescent Cell Viability Assay). Luminescence was read after 2 minutes shaking on an orbital shaker and 10 min incubation at RT using the GloMax instrument (Promega, Madison, USA).

SARS-CoV-2 VSV pseudotype virus assay

Mono-DARPin molecules and multi-DARPin molecules were assessed for inhibition potency in a SARS-CoV-2 VSV pseudotype virus assay. Assays were performed in two different laboratories

Laboratory 1: screening and RBD-competition assays (Tabel 1, Table 2, Figure 4b)

SARS-CoV-2 pseudoviruses were generated as described previously[34]. For the pseudovirus neutralization assay (PsV NA) an initial dilution of the drug was followed by two-fold dilutions in quadruplicates in Dulbecco modified Eagle medium (DMEM)-2 % [vol/vol] fetal calf serum (FCS) The mixture was mixed with an equal volume of medium containing 200 or 2000 infectious units (IU) per well and incubated for 90 min at 37°C. Following this incubation, the mix was inoculated onto Vero E6 cells in a clear bottom white walled 96-well plate during 90 min at 37°C. The inoculum was removed and fresh medium added, and cells further incubated at 37°C for 16 h. Cell were lysed according to the ONE-Glo™ luciferase assay system (Promega, Madison, US) and light emission was recorded using a Berthold® TriStar LB941 luminometer. The raw data (relative light unit values) were exported to GraphPad Prism v8.01, and the % neutralization data were normalized to the untreated PsV signal. IC_{50} with 95% confidence interval were estimated by model of nonlinear regression fit with settings for log (inhibitor) vs normalized response curves.

Laboratory 2: PsV NA for titration curves (Figure 4a)

Production of VSV pseudotyped with SARS2-S was described previously[35]. Briefly, HEK-293T cells were transfected with pCAGGS expression vectors encoding MERS-S, SARS-S or SARS2-S carrying a 16-, 28- or 18-a.a. cytoplasmic tail truncation, respectively. One day post transfection, cells were infected with the VSV-G pseudotyped VSVΔG bearing the firefly (Photinus pyralis) luciferase reporter gene. Twenty-

bioRxiv preprint doi: https://doi.org/10.1101/2020.08.25.256339; this version posted August 26, 2020. The copyright holder for this preprint (which was not certified by peer review) is the author/funder, who has granted bioRxiv a license to display the preprint in perpetuity. It is made available under aCC-BY-NC-ND 4.0 International license.

four hours later, supernatants containing SARS2-S pseudotyped VSV particles were harvested and titrated on African green monkey kidney Vero E6 (ATCC#CRL-1586) cells.

In the virus neutralization assay, DARPin molecules were threefold serially diluted at two times the desired final concentration in DMEM supplemented with 10 µM human serum albumin (CSL Behring), 100 U/ml Penicillin and 100 µg/ml Streptomycin (Lonza). Monoclonal antibodies against MERS-S (2), SARS-S or SARS2-S were included as a positive control[35]. Diluted DARPin molecules and mAbs were incubated with an equal volume of pseudotyped VSV particles for 1 hour at room temperature, inoculated on confluent Vero E6 monolayers in 96-well plate, and further incubated at 37 °C for 24 hours. Cells were lysed with Luciferase Cell Culture Lysis 5X Reagent (Promega) at room temperature for 30 min. Luciferase activity was measured on a Berthold Centro LB 960 plate luminometer using D-luciferin as a substrate (Promega). The half maximal inhibitory concentrations (IC_{50}) were determined using 4-parameter logistic regression (GraphPad Prism version 8).

Cryo-electron microscopy

4 µl of purified S ectodomain (9 µM) was mixed with 1 µl of 50 µM mono-DAPRin #3, #9 or #10, and incubated for 15 seconds at room temperature. 3 µl of sample was then dispensed on Quantifoil R1.2/1.3 200-mesh grids (Quantifoil Micro Tools GmbH) that had been freshly glow discharged for 30 s at 20 mA. Grids were blotted for 5 s using Whatman No. 1 filter paper and immediately plunge-frozen into liquid ethane cooled by liquid nitrogen using a Vitrobot Mark IV plunger (Thermo Fisher Scientific) equilibrated to ~95% relative humidity, 4°C. Movies of frozen-hydrated specimens were collected using Glacios Cryo-TEM (Thermo Fisher Scientific) operating at 200 keV and equipped with a Falcon 4 Direct Electron Detector (Thermo Fisher Scientific). For additional analysis of mono-DARPin #3, 4 µl of purified S ectodomain (18 µM) was mixed with 1 µl of 100 µM DARPin, and incubated for 60 s at room temperature. Grids were prepared as described above, and movies were collected using a Titan Krios Cryo-TEM (Thermo Fisher Scientific) operating at 300 keV and equipped with a Falcon 4 Direct Electron Detector (Thermo Fisher Scientific). All cryo-EM data were acquired using the EPU 2 software (Thermo Fisher Scientific) with a 30-degree stage tilt to account for preferred orientation of the samples. All movies were collected in electron counting mode at 96,000x corresponding to a calibrated pixel size of 1.1 Å/pix over a defocus range of -1.25 to -2.5 µm.

Image processing

Movie stacks were manually inspected and then imported in Relion version 3.0.1[36]. Drift and gain correction were performed with MotionCor2[37], and GCTF[38] was used to estimate the contrast transfer function for each movie. Particles were automatically picked using a gaussian blob template and Fourier binned (2 x 2) particles were extracted and subjected to a round of 2D classification, ignoring CTFs until the first peak. Particles selected from 2D classification were subject to a round of 3D

bioRxiv preprint doi: https://doi.org/10.1101/2020.08.25.256339; this version posted August 26, 2020. The copyright holder for this preprint (which was not certified by peer review) is the author/funder, who has granted bioRxiv a license to display the preprint in perpetuity. It is made available under aCC-BY-NC-ND 4.0 International license.

classification. Particles belonging to the best class were re-extracted unbinned, 3D auto-refined and post-processed. Iterative rounds of per particle defocus estimation, 3D auto-refinement and post-processing were used to account for the 30-degree stage tilt used during data collection.

Molecular modeling of mono and multi-DARPin molecules

Homology models of mono-DARPin molecules #3 and #9 were generated with Rosetta[39]. The consensus designed ankyrin repeat domain PDB ID:2xee was used as template. Mutations were introduced with RosettaRemodel[40] with fixed backbone, and the structure was refined with RosettaRelax[41]. Forty refined structures were clustered using RosettaCluster with 0.3 Å radius, and the lowest-energy model from the largest cluster served as the final model. These models were then used for fitting domain #3 and #9 into the observed electron density generated from the complex structure of the spike protein.

To facilitate accurate fitting of the DARPin coordinates into their respective cryo-EM maps, difference density of the bound DARPin molecules were produced. For mono-DARPin #3, the atomic coordinates of a fully-open spike ectodomain (PDB ID: 6XCN) were fitted into the EM density using the UCSF Chimera 'fit in map' tool. The Fab component of the model was deleted, and then the 'molmap' command was used to simulate a 7 Å resolution density map. This simulated map was then resampled on the grid of the experimental cryo-EM density map using the 'vop resample' command. The 'vop subtract' command was then used to subtract the value of the simulated map from the experimental map. The 'minRMS' option was used to automatically scale the simulated map to minimize the root-mean-square sum of the resulting subtracted values at grid points within the lowest contour of simulated map. The UCSF Chimera 'fit in map' tool was then used to fit mono-DARPin #3 into the difference density until the correlation between the map and model did not improve any further, and ensuring that the epitope binding surface of the mono-DARPin was orientated towards the spike ectodomain. This workflow was then repeated for mono-DARPin #9, using the fully closed spike coordinates (PDB ID: 6ZGE).

The PDB file with the coordinates of the trimer of domain #3:RBD was used as an input structure for the conceptual modeling of MR-DC bound to the spike ectodomain as shown in Figure 5. In both models, the open RBD domain from PDB ID 6vyb was used to generate three RBDs in the open conformation[13]. For the conceptual modeling of MM-DC a similar approach was used by fitting domain #9 into the observed density of the NTD cryo-EM structure. Additionally, a structurally resolved NTD domain from PDB 7c2l was used[23], and a binding domain model of S2 (#10) was placed manually to a potential interacting site on S2 (non-glycosylated region within reasonable distance from the binding

bioRxiv preprint doi: https://doi.org/10.1101/2020.08.25.256339; this version posted August 26, 2020. The copyright holder for this preprint (which was not certified by peer review) is the author/funder, who has granted bioRxiv a license to display the preprint in perpetuity. It is made available under aCC-BY-NC-ND 4.0 International license.

domain #9, based on linker length). For both structures, HSA binding DARPin models were placed and the linkers between each binding domain were modeled using Rosetta modeling tools[40].

In a last step, the models of mono-DARPin #3:RBD (residues 303-526) and mono-DARPin #9:NTD (residues 14-303) were refined with Rosetta. The structures were pre-relaxed for docking and served as input for local, high-resolution docking with RosettaDock[42] with fixed backbone. Five hundred models were generated and clustered with 1 Å radius (RosettaCluster). Two largest clusters were inspected and the lowest-energy model from more conserved group (i.e., with lower rigid-body perturbation from the input structure) was taken further for additional all-atom refinement with RosettaRelax[41], with protocol optimized for interfaces (InterfaceRelax2019). Fifty models were generated, and the lowest scoring model was selected. This model was used to describe the interactions between DARPin molecules and their target domains.

Hamster pharmacokinetic study

Single-dose intraperitoneally administered dose pharmacokinetic measurements in female hamsters (n = 6 per group) were performed at 160 µg and 1600 µg. Blood samples were collected pre-dose and again at 5 min, 1 h, 4 h, 24 h, 48 h, 72 h, 96 h, and 168 h post-injection. Serum concentrations were determined by sandwich ELISA using RBD as capture reagent and an anti-His-tag antibody as detection reagent and using a standard curve. Pharmacokinetic parameters were determined using the software Phoenix WinNonLin (Certara, Princeton, USA) or GraphPadPrism (GraphPad Software, La Jolla,USA) and non-compartmental analyses.

Prophylactic Golden Syrian hamster model for the assessment of antiviral potency of candidate MR-DC The study was performed at Viroclinics Xplore, Schaijk, The Netherlands.

Virus used for Golden Syrian hamster study

SARS-CoV-2 isolate BetaCoV/Munich/BavPat1/2020 was kindly provided by Prof. Dr. C. Drosten (European Virus Archive Global # 026V-03883). With a history of 1 passage in Vero-TMPRSS2 and 3 passages in Vero E6 cells (ATCC), the seed stock was titrated in Vero E6 cells to a concentration of 7.1 log10 $TCID_{50}$/ml. The seed stock was thawed and diluted in cold phosphate-buffered saline (PBS) prior to infection.

Experimental design

Twenty-four specific-pathogen-free (SPF) 15 weeks-old Golden Syrian hamsters (Mesocricetus auratus, females, provided by Envigo) were uniquely identified using individually-coded animal markers. They were housed in elongated type 2 group cages with two animals per cage under BSL-III conditions during the experiment. They were kept according to the standards of Dutch law for animal experimentation

bioRxiv preprint doi: https://doi.org/10.1101/2020.08.25.256339; this version posted August 26, 2020. The copyright holder for this preprint (which was not certified by peer review) is the author/funder, who has granted bioRxiv a license to display the preprint in perpetuity. It is made available under aCC-BY-NC-ND 4.0 International license.

and were checked daily for overt signs of disease. The study was carried out following approval by an independent animal welfare body (approval AVD277002015283-WP13) and complied with all relevant ethical regulations for animal testing.

Four groups of six hamsters were treated with multi-DARPin molecule MR-DC via the intraperitoneal route with 16 µg, 160 µg, or 1600 µg doses per animal or with a placebo 24 hours prior to infection and subsequently animals were inoculated intra-nasally with 100 µL PBS containing $5x10^4$ $TCID_{50}$ SARS-CoV-2. The inoculum was instilled dropwise using a pipette and equally divided over both nostrils. The animals were weighed regularly and throat swabs, for quantitative PCR and infectious virus titration, were collected on a daily basis. For all animal procedures, the animals were sedated with isoflurane (3-4%/O2).

Upon necropsy at day 4 post infection, full-body gross pathology was assessed for each animal and all abnormalities recorded and described. All lung lobes were inspected, and the percentage of affected lung tissue was estimated by eye. Samples of the left nasal turbinates, trachea and the entire left lung (often with presence of the primary bronchi) were preserved in 10% formaldehyde for histopathology. Samples of the right lung parenchyma and right nasal turbinates were frozen for quantitative PCR and virus titration.

Virology

Throat swabs and homogenized tissue samples (lungs and nasal turbinates) were thawed and tested for the presence of SARS-CoV-2 RNA using RT-qPCR and of infectious virus using virus titration.

RNA was extracted from samples using Magnapure LC total nucleic acid isolation kit (Roche). RNA amplification and quantification were carried out using a 7500 Real-Time PCR System (Applied biosystems) specific primers (E_Sarbeco_F: ACAGGTACGTTAATAGTTAATAGCGT and E_Sarbeco_R: ATATTGCAGCAGTACGCACACA) and probe (E_Sarbeco_P1: ACACTAGCCATCCTTACTGCGCTTCG) as described[43] and RNA copies were calculated.

Quadruplicate 10-fold serial dilutions were used to determine the virus titers on confluent layers of Vero E6 cells. To this end, serial dilutions of the samples (throat swabs and tissue homogenates) were prepared and incubated on Vero E6 monolayers for 1 hour at 37oC. Vero E6 monolayers were washed with PBS and incubated for 4-6 days at 37oC after which plates were scored for cytopathogenic effect (CPE) using the vitality marker WST-8. Viral titers ($TCID_{50}$) were calculated using the method of Spearman-Karber.

Histopathology

After fixation with 10% neutral-buffered formalin, sections of the left lung, left nasal turbinate and trachea were embedded in paraffin. The tissue sections were stained with hematoxylin and eosin (H&E) for histopathological evaluation. Semi-quantitative scores of 0, 1, 2 or 3 were given when the extent of alveolitis and alveolar damage were estimated at 0%; 1–25%; 26–50% or >50%, respectively.

bioRxiv preprint doi: https://doi.org/10.1101/2020.08.25.256339; this version posted August 26, 2020. The copyright holder for this preprint (which was not certified by peer review) is the author/funder, who has granted bioRxiv a license to display the preprint in perpetuity. It is made available under aCC-BY-NC-ND 4.0 International license.

The cumulative score for the extent and severity of inflammation of the lung provided the total score of alveolitis per animal. For the severity of alveolitis, bronchiolitis, bronchitis, and tracheitis, semi-quantitative scores of 0, 1, 2 or 3 were given when no, few, moderate numbers or many inflammatory cells were present, respectively. For the presence of alveolar edema, alveolar hemorrhage, and type II pneumocyte hyperplasia, scores of 0 or 1 were given upon their absence or presence, respectively. For the extent of peribronchial, peribronchiolar, and perivascular infiltrates, semi-quantitative scores of 0, 1, 2 or 3 were given when infiltrates were absent, or when they were one to two, three to ten, or more than ten cells thick, respectively.

bioRxiv preprint doi: https://doi.org/10.1101/2020.08.25.256339; this version posted August 26, 2020. The copyright holder for this preprint (which was not certified by peer review) is the author/funder, who has granted bioRxiv a license to display the preprint in perpetuity. It is made available under aCC-BY-NC-ND 4.0 International license.

Supplementary Figures

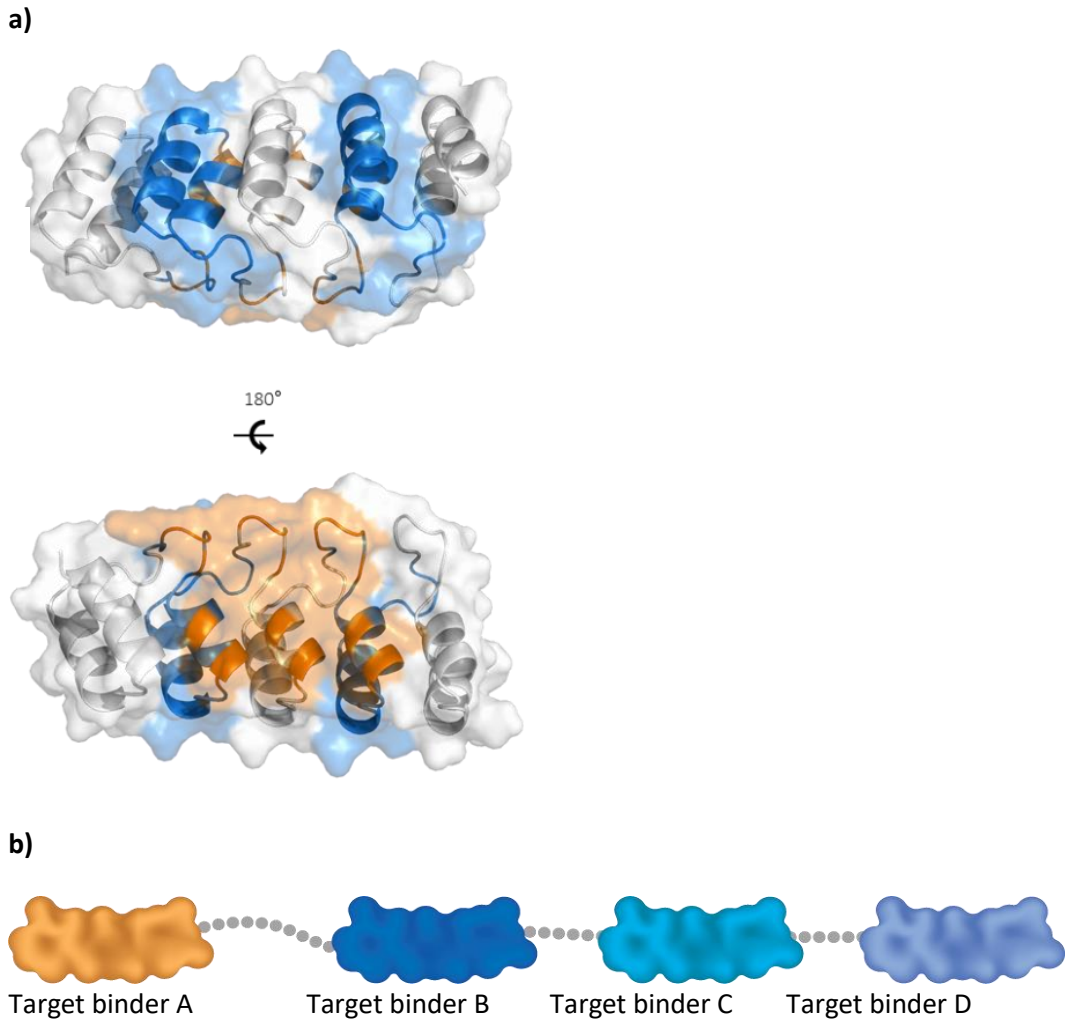

Supplementary Figure 1: a) Mono-DARPin molecule shown as ribbon structure and designed ankyrin repeats are colored alternatingly in white and blue for the five repeats. Different to flexible CDR loops of antibodies, target binding occurs via a rigid surface using randomized residues colored in orange. b) DARPin modality: mono-DARPin molecules may be linked with standard protein linkers (grey bead-string) to generate bi-specific up to, at least, hexa-specific multi-DARPin molecules (here a tetra-specific DARPin molecule is illustrated). While incorporating various and additive modes of action in a single chain construct (e.g. adding a human serum albumin binder for half-life extension or binding of various targets respectively target domains), these multi-DARPin molecules maintain their class behavior such as high binding affinities, biophysical properties which allow rapid drug development or excellent protein expression yields in bacterial cultures.

bioRxiv preprint doi: https://doi.org/10.1101/2020.08.25.256339; this version posted August 26, 2020. The copyright holder for this preprint (which was not certified by peer review) is the author/funder, who has granted bioRxiv a license to display the preprint in perpetuity. It is made available under aCC-BY-NC-ND 4.0 International license.

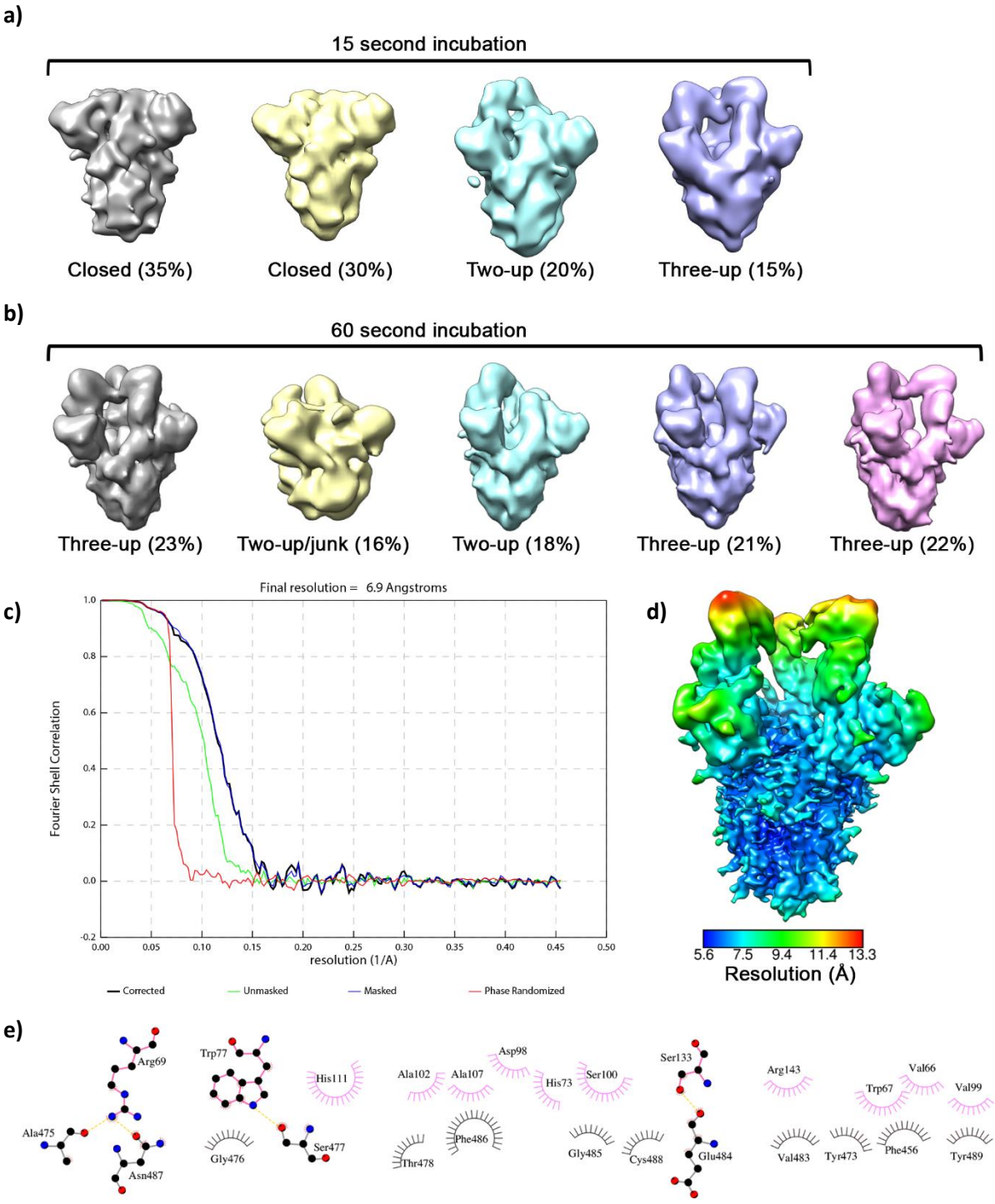

Supplementary Figure 2: a) 3D classes obtained from spike ectodomains incubated with mono-DARPin #3 for 15 seconds, and b) for 60 seconds. c) Gold-standard Fourier shell correlation (FSC) curve generated from the independent half maps contributing to the 6.9 Å resolution density map. d) The EM density map of the spike ectodomain bound to three copies of mono-DARPin #3, coloured according to local resolution. e) DimPlot[44] representation of putative interacting residues between the spike ectodomain RBD and mono-DARPin #3, identified through molecular docking experiments. Residues participating in hydrophobic interactions are shown as spoke arcs. Residues participating in hydrogen bonding are shown as sticks, and hydrogen bonds are shown as yellow dotted lines. Residues are coloured grey and pink for spike and PDB #3, respectively.

bioRxiv preprint doi: https://doi.org/10.1101/2020.08.25.256339; this version posted August 26, 2020. The copyright holder for this preprint (which was not certified by peer review) is the author/funder, who has granted bioRxiv a license to display the preprint in perpetuity. It is made available under aCC-BY-NC-ND 4.0 International license.

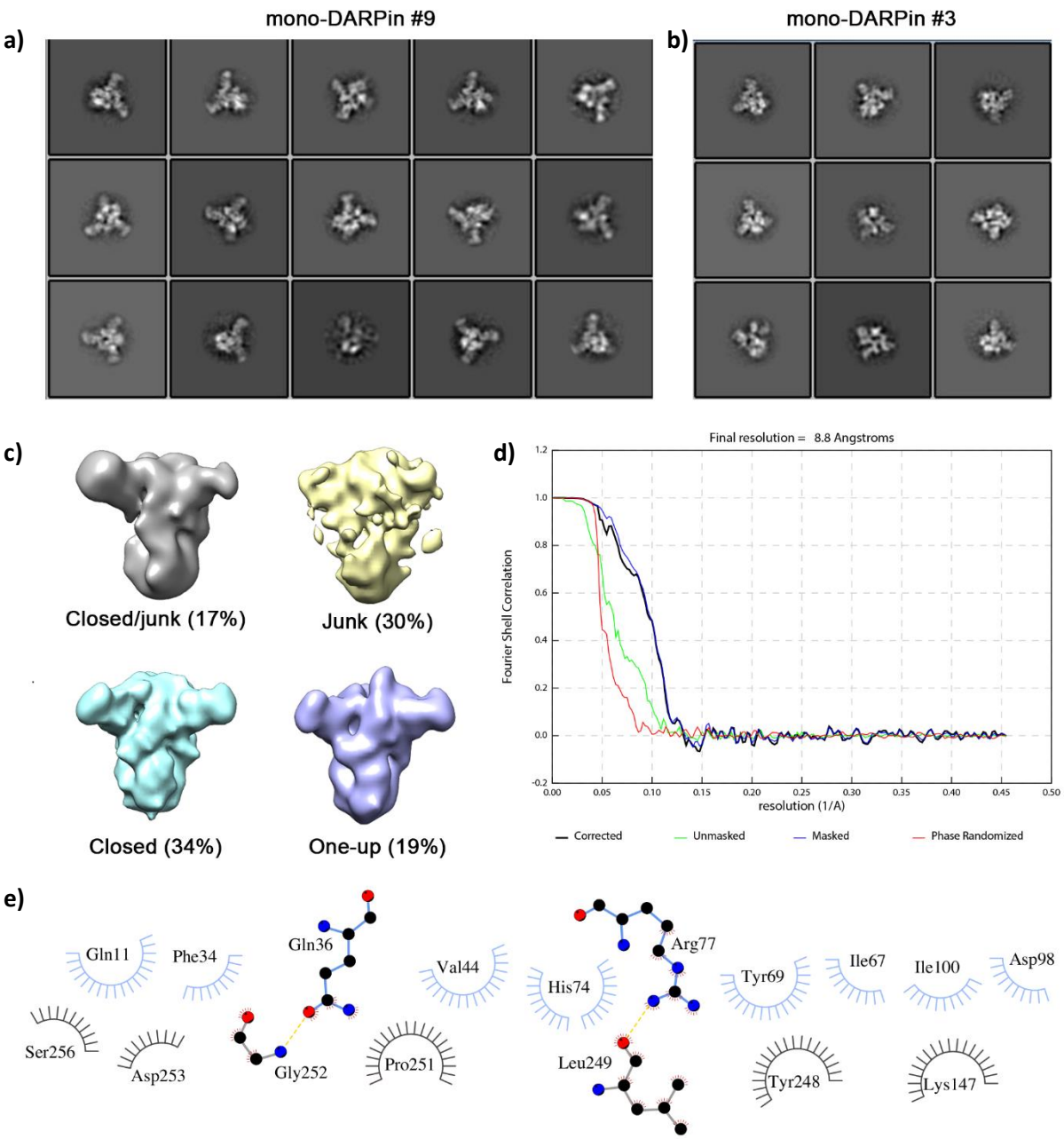

Supplementary Figure 3 a) Representative reference-free 2D class averages obtained from the mono-DARPin #9 incubated spike ectodomains, and b) mono-DAPRin #3 incubated samples, shown for comparison. c) 3D classes obtained from spike ectodomains incubated with mono-DARPin #3 for 15 seconds. d) Gold-standard Fourier shell correlation (FSC) curve generated from the independent half maps contributing to the 8.8 Å resolution density map. e) DimPlot[44] representation of putative interacting residues between the spike ectodomain NTD and mono-DARPin #9, identified through molecular docking experiments. Residues participating in hydrophobic interactions are shown as spoke arcs. Residues participating in hydrogen bonding are shown as sticks, and hydrogen bonds are shown as yellow dotted lines. Residues are coloured grey and blue for spike and monoDARPin #9, respectively.

bioRxiv preprint doi: https://doi.org/10.1101/2020.08.25.256339; this version posted August 26, 2020. The copyright holder for this preprint (which was not certified by peer review) is the author/funder, who has granted bioRxiv a license to display the preprint in perpetuity. It is made available under aCC-BY-NC-ND 4.0 International license.

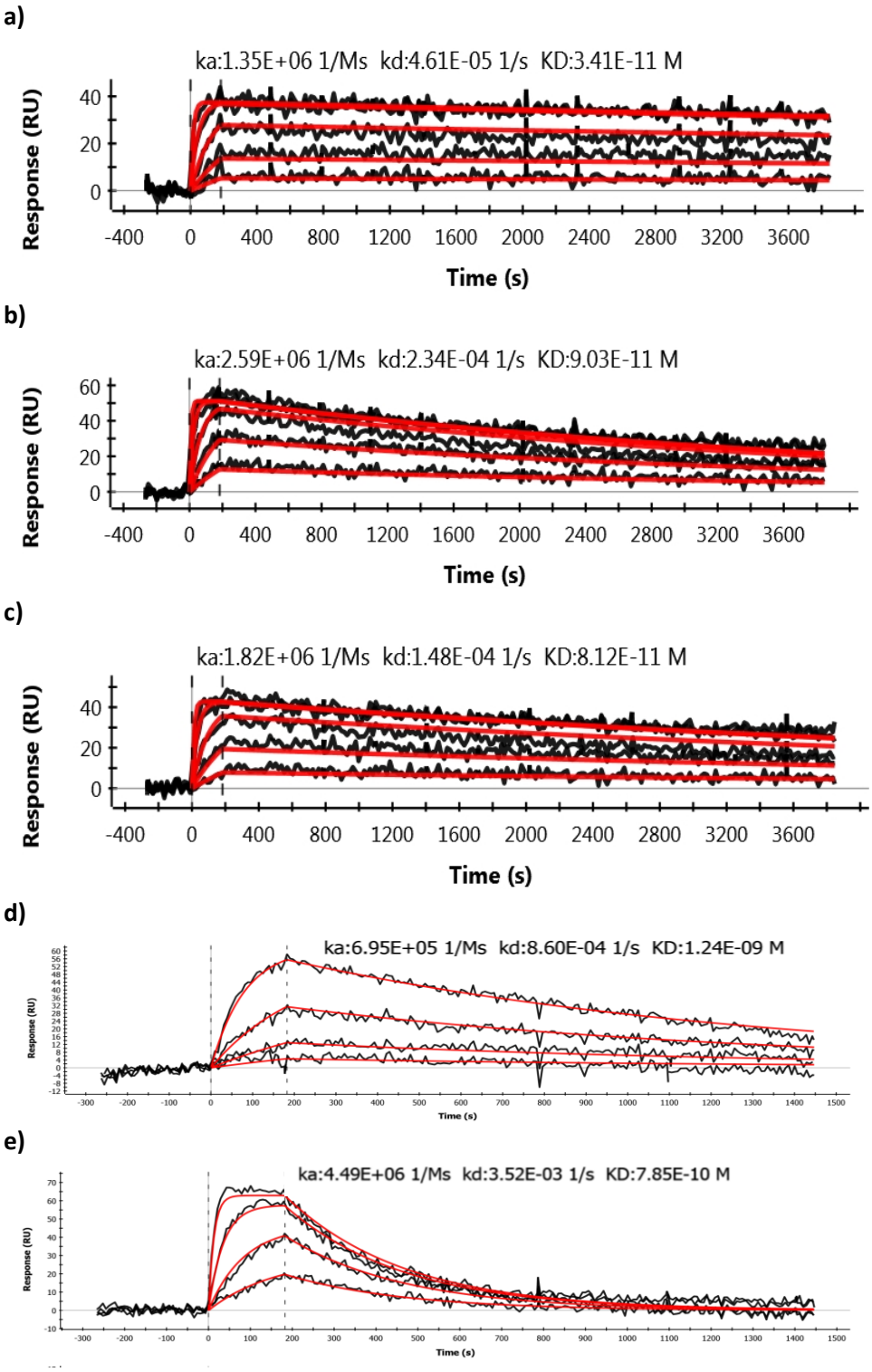

Supplementary Figure 4: Surface plasmon resonance (SPR) sensorgrams of the mono-DARPin molecules #3, #5, #6, #9, #10, incorporated in MR-DC. a-c) and MM-DC (c-e) binding to immobilized trimeric spike protein. DARPin concentrations for a-c: 50/16.67/5.56/1.85/0.62 nM. DARPin concentrations for (d) and (e): 16.67/5.56/1.85/0.62 nM. Affinity values of mono-DARPin molecules are listed in **Table 1**.

bioRxiv preprint doi: https://doi.org/10.1101/2020.08.25.256339; this version posted August 26, 2020. The copyright holder for this preprint (which was not certified by peer review) is the author/funder, who has granted bioRxiv a license to display the preprint in perpetuity. It is made available under aCC-BY-NC-ND 4.0 International license.

References

1 Zhou, P. *et al.* A pneumonia outbreak associated with a new coronavirus of probable bat origin. *Nature* **579**, 270-273, doi:10.1038/s41586-020-2012-7 (2020).

2 Hsiang, S. *et al.* The effect of large-scale anti-contagion policies on the COVID-19 pandemic. *Nature* **584**, 262-267, doi:10.1038/s41586-020-2404-8 (2020).

3 Flaxman, S. *et al.* Estimating the effects of non-pharmaceutical interventions on COVID-19 in Europe. *Nature* **584**, 257-261, doi:10.1038/s41586-020-2405-7 (2020).

4 Guy, R. K., DiPaola, R. S., Romanelli, F. & Dutch, R. E. Rapid repurposing of drugs for COVID-19. *Science* **368**, 829-830, doi:10.1126/science.abb9332 (2020).

5 Ledford, H. Antibody therapies could be a bridge to a coronavirus vaccine - but will the world benefit? *Nature* **584**, 333-334, doi:10.1038/d41586-020-02360-y (2020).

6 Binz, H. K. *et al.* High-affinity binders selected from designed ankyrin repeat protein libraries. *Nat Biotechnol* **22**, 575-582, doi:10.1038/nbt962 (2004).

7 Pinto, D. Cross-neutralization of SARS-CoV-2 by a human monoclonal SARS-CoV antibody. (2020).

8 Baum, A. *et al.* Antibody cocktail to SARS-CoV-2 spike protein prevents rapid mutational escape seen with individual antibodies. *Science*, doi:10.1126/science.abd0831 (2020).

9 Hansen, J. *et al.* Studies in humanized mice and convalescent humans yield a SARS-CoV-2 antibody cocktail. *Science*, doi:10.1126/science.abd0827 (2020).

10 Shang, J. *et al.* Structural basis of receptor recognition by SARS-CoV-2. *Nature* **581**, 221-224, doi:10.1038/s41586-020-2179-y (2020).

11 Tortorici, M. A. & Veesler, D. Structural insights into coronavirus entry. *Adv Virus Res* **105**, 93-116, doi:10.1016/bs.aivir.2019.08.002 (2019).

12 Walls, A. C. *et al.* Cryo-electron microscopy structure of a coronavirus spike glycoprotein trimer. *Nature* **531**, 114-117, doi:10.1038/nature16988 (2016).

13 Walls, A. C. *et al.* Structure, Function, and Antigenicity of the SARS-CoV-2 Spike Glycoprotein. *Cell* **181**, 281-292 e286, doi:10.1016/j.cell.2020.02.058 (2020).

14 Zahnd, C., Amstutz, P. & Pluckthun, A. Ribosome display: selecting and evolving proteins in vitro that specifically bind to a target. *Nat Methods* **4**, 269-279, doi:10.1038/nmeth1003 (2007).

15 Hanes, J., Jermutus, L., Weber-Bornhauser, S., Bosshard, H. R. & Pluckthun, A. Ribosome display efficiently selects and evolves high-affinity antibodies in vitro from immune libraries. *Proc Natl Acad Sci U S A* **95**, 14130-14135, doi:10.1073/pnas.95.24.14130 (1998).

16 Binz, H. K., Stumpp, M. T., Forrer, P., Amstutz, P. & Pluckthun, A. Designing repeat proteins: well-expressed, soluble and stable proteins from combinatorial libraries of consensus ankyrin repeat proteins. *J Mol Biol* **332**, 489-503, doi:10.1016/s0022-2836(03)00896-9 (2003).

17 Walls, A. C. *et al.* Unexpected Receptor Functional Mimicry Elucidates Activation of Coronavirus Fusion. *Cell* **176**, 1026-1039 e1015, doi:10.1016/j.cell.2018.12.028 (2019).

18 Niesen, F. H., Berglund, H. & Vedadi, M. The use of differential scanning fluorimetry to detect ligand interactions that promote protein stability. *Nat Protoc* **2**, 2212-2221, doi:10.1038/nprot.2007.321 (2007).

bioRxiv preprint doi: https://doi.org/10.1101/2020.08.25.256339; this version posted August 26, 2020. The copyright holder for this preprint (which was not certified by peer review) is the author/funder, who has granted bioRxiv a license to display the preprint in perpetuity. It is made available under aCC-BY-NC-ND 4.0 International license.

19 Barnes, C. O. *et al.* Structures of Human Antibodies Bound to SARS-CoV-2 Spike Reveal Common Epitopes and Recurrent Features of Antibodies. *Cell*, doi:10.1016/j.cell.2020.06.025 (2020).

20 Wrapp, D. *et al.* Cryo-EM structure of the 2019-nCoV spike in the prefusion conformation. *Science* **367**, 1260-1263, doi:10.1126/science.abb2507 (2020).

21 Wrobel. SARS-CoV-2 and bat RaTG13 spike glycoprotein structures inform on virus evolution and furin-cleavage effects. (2020).

22 Cai, Y. Distinct conformational states of SARS-CoV-2 spike protein. (2020).

23 Chi, X. *et al.* A neutralizing human antibody binds to the N-terminal domain of the Spike protein of SARS-CoV-2. *Science* **369**, 650-655, doi:10.1126/science.abc6952 (2020).

24 Stumpp, M. T., Dawson, K. M. & Binz, H. K. Beyond Antibodies: The DARPin((R)) Drug Platform. *BioDrugs* **34**, 423-433, doi:10.1007/s40259-020-00429-8 (2020).

25 Brouwer, P. J. M. *et al.* Potent neutralizing antibodies from COVID-19 patients define multiple targets of vulnerability. *Science* **369**, 643-650, doi:10.1126/science.abc5902 (2020).

26 Liu, L. *et al.* Potent neutralizing antibodies against multiple epitopes on SARS-CoV-2 spike. *Nature* **584**, 450-456, doi:10.1038/s41586-020-2571-7 (2020).

27 Rogers, T. F. *et al.* Isolation of potent SARS-CoV-2 neutralizing antibodies and protection from disease in a small animal model. *Science*, doi:10.1126/science.abc7520 (2020).

28 Shi, R. *et al.* A human neutralizing antibody targets the receptor-binding site of SARS-CoV-2. *Nature* **584**, 120-124, doi:10.1038/s41586-020-2381-y (2020).

29 Zost, S. J. *et al.* Potently neutralizing and protective human antibodies against SARS-CoV-2. *Nature* **584**, 443-449, doi:10.1038/s41586-020-2548-6 (2020).

30 Schoof, M. *et al.* An ultra-high affinity synthetic nanobody blocks SARS-CoV-2 infection by locking Spike into an inactive conformation. *bioRxiv*, doi:10.1101/2020.08.08.238469 (2020).

31 Fiedler, U. *et al.* MP0250, a VEGF and HGF neutralizing DARPin((R)) molecule shows high anti-tumor efficacy in mouse xenograft and patient-derived tumor models. *Oncotarget* **8**, 98371-98383, doi:10.18632/oncotarget.21738 (2017).

32 Mulangu, S. *et al.* A Randomized, Controlled Trial of Ebola Virus Disease Therapeutics. *N Engl J Med* **381**, 2293-2303, doi:10.1056/NEJMoa1910993 (2019).

33 Binz, H. K. *et al.* Design and characterization of MP0250, a tri-specific anti-HGF/anti-VEGF DARPin(R) drug candidate. *MAbs* **9**, 1262-1269, doi:10.1080/19420862.2017.1305529 (2017).

34 Torriani, G. *et al.* Macropinocytosis contributes to hantavirus entry into human airway epithelial cells. *Virology* **531**, 57-68, doi:10.1016/j.virol.2019.02.013 (2019).

35 Wang, C. *et al.* A human monoclonal antibody blocking SARS-CoV-2 infection. *Nat Commun* **11**, 2251, doi:10.1038/s41467-020-16256-y (2020).

36 Zivanov, J. *et al.* New tools for automated high-resolution cryo-EM structure determination in RELION-3. *Elife* **7**, doi:10.7554/eLife.42166 (2018).

37 Zheng, S. Q. *et al.* MotionCor2: anisotropic correction of beam-induced motion for improved cryo-electron microscopy. *Nat Methods* **14**, 331-332, doi:10.1038/nmeth.4193 (2017).

38 Zhang, K. Gctf: Real-time CTF determination and correction. *J Struct Biol* **193**, 1-12, doi:10.1016/j.jsb.2015.11.003 (2016).

bioRxiv preprint doi: https://doi.org/10.1101/2020.08.25.256339; this version posted August 26, 2020. The copyright holder for this preprint (which was not certified by peer review) is the author/funder, who has granted bioRxiv a license to display the preprint in perpetuity. It is made available under aCC-BY-NC-ND 4.0 International license.

39 Leaver-Fay, A. *et al.* ROSETTA3: an object-oriented software suite for the simulation and design of macromolecules. *Methods Enzymol* **487**, 545-574, doi:10.1016/B978-0-12-381270-4.00019-6 (2011).

40 Huang, P. S. *et al.* RosettaRemodel: a generalized framework for flexible backbone protein design. *PLoS One* **6**, e24109, doi:10.1371/journal.pone.0024109 (2011).

41 Nivon, L. G., Moretti, R. & Baker, D. A Pareto-optimal refinement method for protein design scaffolds. *PLoS One* **8**, e59004, doi:10.1371/journal.pone.0059004 (2013).

42 Chaudhury, S. *et al.* Benchmarking and analysis of protein docking performance in Rosetta v3.2. *PLoS One* **6**, e22477, doi:10.1371/journal.pone.0022477 (2011).

43 Corman, V. M. *et al.* Detection of 2019 novel coronavirus (2019-nCoV) by real-time RT-PCR. *Euro Surveill* **25**, doi:10.2807/1560-7917.ES.2020.25.3.2000045 (2020).

44 Laskowski, R. A. & Swindells, M. B. LigPlot+: multiple ligand-protein interaction diagrams for drug discovery. *J Chem Inf Model* **51**, 2778-2786, doi:10.1021/ci200227u (2011).